Experimental exploration of digitally fabricated connections for structural concrete

Patrick Bischof [a,*], Jaime Mata-Falcón [a], Joris Burger [b], Lukas Gebhard [a], Walter Kaufmann [a]

[a] Institute of Structural Engineering, Department of Civil, Environmental and Geomatic Engineering, ETH Zurich, Switzerland
[b] Institute of Technology in Architecture, Department of Architecture, ETH Zurich, Switzerland

ARTICLE INFO

ABSTRACT

Connections are a persistent challenge for traditional reinforced concrete construction and even more for digital fabrication with concrete (DFC). The latter, on the other hand, opens up new possibilities for producing connections with tailored geometries and surface roughness. Based on the findings of an exploratory, experimental campaign, this paper discusses the design, fabrication and structural testing of digitally fabricated joints using the DFC technology *Eggshell* to 3D print the formwork for joint surfaces in an additive manufacturing process. The programme includes (i) unreinforced and reinforced construction joints whose joint surface texture was varied to control the roughness and (ii) digitally fabricated dry keyed joints with varying geometry. Both, the construction joints as well as the dry keyed joints, were produced using set-on-demand concrete with a relatively small maximum aggregate size of 0 to 4 mm – i.e., strictly speaking, mortar rather than concrete – as typically applied in DFC. The experimental campaign included thorough instrumentation: a 3D scan of the joint surface before testing and high-resolution digital image correlation (DIC) combined with distributed fibre optical sensing (DFOS) during testing. The deviations from the targeted surface geometry, determined with 3D scans, were below 2 mm, with a standard deviation between 0.4 mm and 0.7 mm for keyed joints. The high-resolution DIC allowed measuring the compressive strains locally at (i) the corrugation of unreinforced or reinforced construction joints and (ii) the key chamfer of dry joints and, hence, studying strain variations over the height of the joints and the efficiency of different keys with varying dimensions. Finally, the shear transfer capacity, evaluated in a push-off test setup, showed that all digitally fabricated joints met or even outperformed the requirements defined in pertinent design codes despite the smaller aggregate size.

1. Introduction

Connections are highly relevant for both the construction process and the structural behaviour of concrete structures. Particularly for prefabricated construction, they represent "one major key" [1]. This comment applies all the more to the emerging field of digital fabrication with concrete (DFC), which encompasses various fabrication methods directly following model data [2] and supporting the construction of structures, members or parts thereof, promising to enhance the feasibility of economically creating shapes to foster sustainable, material-optimised construction (e.g. see Wangler et al. [3]): These new technologies strongly rely on prefabricated elements, as the fabrication processes rely on a controlled environment and typically involves small elements with material-optimising geometries (e.g. see [4–8]). Therefore, structural connections are paramount to the success of DFC in large-scale load-bearing applications.

Connections consist of one or several joints, each with two surfaces in contact, where forces (e.g. tension, shear, compression), bending moments or both are transferred [1]. They result from (i) staged construction of monolithic structures, (ii) partial prefabrication, or (iii) joining fully precast elements (e.g. see *fib* Bulletin 74 [9]). Note that although the force transfer across construction joints is often taken for granted in design, they are essentially connections, and specific measures are required on site to ensure the presumed monolithic behaviour. Fig. 1 shows several applications of reinforced construction joints (Fig. 1a-c), unreinforced construction joints (Fig. 1d and 1e), or keyed joints (Fig. 1f-h). Construction joints incorporate a typically roughened or corrugated concrete-to-concrete interface with new concrete (dark green fillings in Fig. 1) cast against existing concrete (light green fillings in Fig. 1). Connections of two precast elements often incorporate added

---
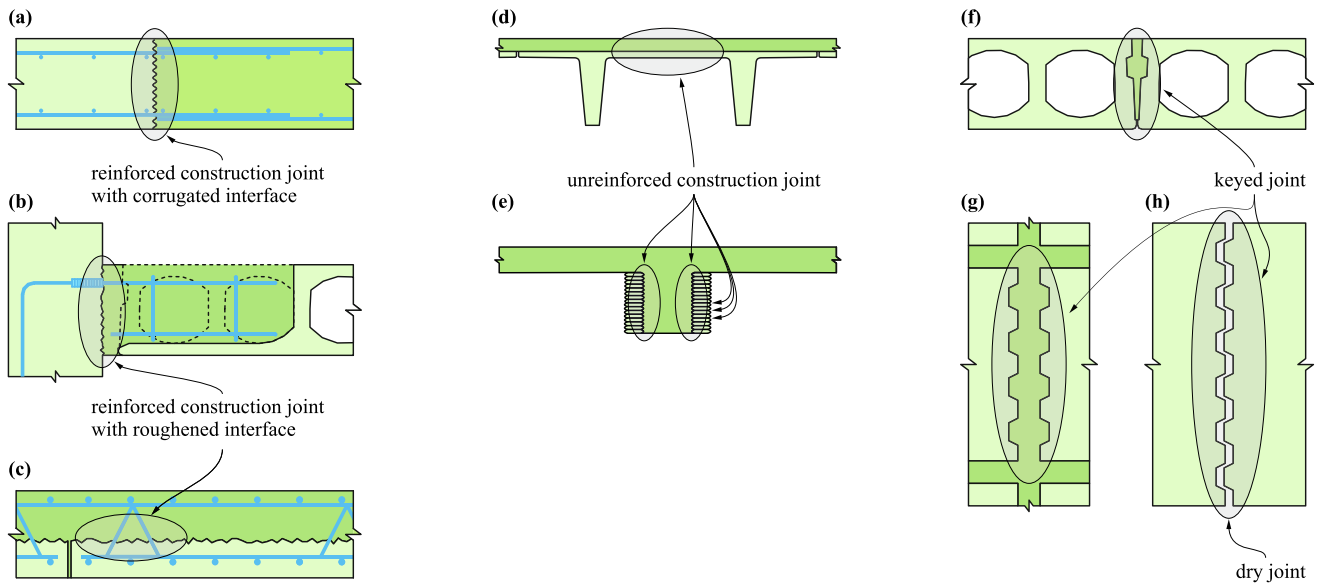
Fig. 1. Details of common connections in concrete structures: (a) typical reinforced construction joint between two construction steps; (b) reinforced construction joint to connect a Hollow-Core Slab to a wall; (c) reinforced construction joint between precast elements and an on-site topping; (d) unreinforced construction joint between precast elements and an on-site topping; (e) unreinforced construction joint between a prefabricated lost printed formwork and cast concrete; (f) keyed joint between two Hollow-Core slabs; (g) keyed joint between wall segments; (h) dry keyed joints typically used in segmental bridging.

on-site concrete or mortar and are considered as wet keyed joints (Fig. 1f and 1g). In dry keyed joints, precast elements are assembled without on-site concrete (Fig. 1h). Note that if the latter is combined with adhesives (such as epoxy resin), they are commonly refereed to as epoxy joints, which are not discussed in this paper.

Production constraints for connections often dictate the design of conventionally built structures. The execution of connections involves a disproportionate amount of manual labour and is decisive for the behaviour and load-bearing capacity of the joints and the overall structure [10]. Continuous reinforcement in construction joints typically requires reinforcing bars penetrating the stop-end formwork, i.e., on-site mounting of bars through the plywood, using stay-in-place mesh grids (susceptible to durability issues) or preparing time- and cost-inefficient bespoke formwork pieces. Post-processing operations for construction joints to ensure appropriate surface roughness, such as cleaning, high-pressure water-jetting, milling, shot-blasting or sand-blasting, may be time-consuming, increasingly with higher concrete strength [11]. Furthermore, operations required to ensure fitting keyed joints limit the number of elements cast per day (match-casting) or represent manual works on-site (grouting).

Connections are equally challenging for many DFC processes. For example, Nuh et al. [6] had to modify manually each segment of their structurally optimised floor slab due to tolerance issues of the timber formwork. Anton et al. [5] either cut the contact surfaces to generate fitting dry joints or filled joints with mortar (i.e., used wet joints) to accommodate the geometrical imperfections of the 3D printing process. Deviations from the theoretical shape were due to (i) the positioning of the robot, (ii) deformations occurring after the material extrusion and (iii) the typically stepped surface texture characteristic of the layered deposition. Burger et al. [7] realised and tested a 2.7 m × 2.7 m part of a material-optimised ribbed floor slab using 3D printed formwork but did not address the challenge of joining multiple elements.

On the other hand, DFC may be exploited to explore new options for producing structural connections by shaping tailored contact surfaces [12,13]. The geometrical flexibility of DFC can be used to provide construction joints with a controlled profiled texture. Furthermore, DFC may ease the execution of construction joints with continuous reinforcement by placing reinforcing bars or meshes perpendicular to

additively printed stay-in-place stop-end formwork pieces. Additive DFC technologies providing high geometrical precision may also be used to flexibly shape fitting keyed joints without the need for match-casting. The same result could also be achieved by means of robotically-controlled milling processes, which have been explored in DFC processes not only on hardened concrete but also on green-state concrete, aiming at (i) increasing the processing speed and (ii) reducing tool wear [14,15].

The advantages of geometrical flexibility and high spatial precision (small tolerance requirements) with additive or subtractive (e.g green-state milling) shaping processes depend on the use of concrete with small maximum aggregates – 0…4 mm in this study – as typically applied in DFC. Such mixes are conventionally designated as mortar rather than concrete. The small aggregate size may affect the mechanical properties and hence, the behaviour of the joints. For example, Nielsen [16] and Sørensen [17] found that the beneficial effect of lateral compression on the triaxial concrete compressive strength was less pronounced for mortar than for concrete. Furthermore, several recent studies using mortars within the framework of digital fabrication at ETH Zurich [18–20] indicated that the ratio of tensile to compressive strength might be lower for the used material than for typical concrete, which is particularly relevant for unreinforced joints, whose behaviour strongly depends on the concrete tensile strength. However, research on joints with mortar is comparably scarce, as pointed out by Sørensen [17], who studied the behaviour of keyed joints with reinforcement crossing the joint and with keys of mortar instead of concrete. Sørensen's main research focus was, though, on joints under combined shear and tensile loading, which is not elaborated on in this paper.

This paper explores new possibilities offered by DFC to produce different joint configurations by means of an experimental campaign, including the design, fabrication and structural testing of reinforced and unreinforced construction joints with varying surface textures as well as fitting keyed joints using shear keys with varying dimensions in height, depth and key chamfer angle. The campaign serves to (i) explore new possibilities and corresponding challenges for designing and fabricating digitally fabricated joints, (ii) investigate their behaviour under shear loading and (iii) discuss their performance compared to traditional joints and the applicability of code provisions. All specimens were made

of concrete with aggregates of 0–4 mm, cast in formworks produced using the DFC technology *Eggshell* [21], a concrete prefabrication process that uses robotic fused deposition modelling (FDM) 3D printing of thin additive plastic formworks. The technology developed within the framework of the National Competence Centre for Digital Fabrication (NCRR dfab) at ETH Zurich comprises two approaches: (i) printing slender formworks for simultaneous or subsequent casting using a fast-hardening, set-on-demand concrete [21,22]; (ii) printing formwork with stiffening ribs for casting using standard concrete [7]. This study used the first approach with subsequent casting. The *Eggshell* FDM 3D printing allows designing a formwork defining the surface texture of a joint without extra effort compared to a straight contact surface, (i) globally with the printed geometry (resolution > 2 mm) and (ii) locally with the direction of the thermoplastic filament used to print the formwork (resolution ≈ 0.5…2 mm, depending on the filament). Moreover, reinforcement can be complemented where necessary while additively producing the layered formwork – this idea was applied by Burger et al. [7]. Finally, the accuracy of FDM 3D printing is relatively easy to control, entailing the possibility of printing joints with high geometrical precision.

2. Structural connections

Structural connections transfer compressive, shear and tensile forces between adjacent structures, members, or parts thereof (e.g. between lost formwork and a topping). The following sections serve as a basis for understanding the behaviour of joints transferring shear forces (i.e., forces acting parallel to the joint) by providing (i) a short overview of the mechanical behaviour and design concepts and (ii) selected references out of the numerous studies in the field, both without claim for completeness.

2.1. Mechanical behaviour of structural connections under shear loading

The shear transfer across interfaces in concrete structures has been the subject of many studies, with seminal works published more than five decades ago [23–25]. An overview of the most relevant works was presented by Randl [26], summarising the findings of previous and ongoing studies in the field. Accordingly, the transfer of shear forces can be attributed to several contributions: (i) adhesion and mechanical interlock, (ii) friction and (iii) reinforcement crossing the joint (where applicable). Adhesion and mechanical interlock are effective at very small joint slips (<0.05 mm [26]). Adhesion comprises chemical as well as physical bonding and depends on the texture of the contact surface, commonly recognised as roughness [27]. A mechanical interlock can be activated with a high surface roughness ($R_t \geq 1.5$ mm [26], with R_t = mean texture depth according to Kaufmann [28]). Friction depends on the interface roughness as well as acting compressive force; it can be interpreted as an inclination of compressive forces acting on the joint. Reinforcement crossing a joint should have a ratio of at least 0.05% to be effectively engaged, according to the *fib* model code 2010 [10]. If shear forces are transferred across a joint, the reinforcement undergoes bending moments (generally referred to as "dowel action") at slips of approximately 0.5…1.5 mm [26], where the reinforcement is also activated in tension, giving rise to compressive forces acting in the joint enabling shear transfer by friction [29].

The shear transfer capacity of construction joints depends on the slip (e.g. [29]), making it impossible to separate the contributions of adhesion and mechanical interlock, friction and reinforcement, respectively. Generally, adhesion and mechanical interlock govern the shear transfer capacity at low slip values. In contrast, friction, including the effects of reinforcement crossing the joint, controls the shear transfer capacity at higher slip values. The surface texture is decisive for the magnitude of each contribution and, accordingly, the load–displacement behaviour of the joint. For example, a high roughness implies a stiff reaction and brittle failure unless reinforcement crossing the joint (activated at

higher slip) provides a higher resistance than adhesion and the mechanical interlock, acting at small slip values. The behaviour of a joint depends not only on its mean texture depth but also on its detailed surface texture, which according to Tirassa et al. [30] can be described by parameters related to (i) the *micro*-roughness at the scale of the concrete matrix (typically between 1/10 and 1/100 of the maximum aggregate size), (ii) the *meso*-roughness at the scale of the maximum aggregate size and (iii) the *macro*-roughness at the scale of global crack or joint geometry.

The load-deformation behaviour and strength of construction joints lacking sufficient reinforcement is subjected to considerable scatter due to (i) the high dependency on the material properties and (ii) the variations caused by manual labour involved in the preparation of joints. Stress concentrations at the edge zones of contact surfaces, highly relevant when adhesion and mechanical interlock prevail (e.g. see [26,31]), increase the dependency of joints on good execution quality. Furthermore, creep and shrinkage of existing old concrete and added new concrete can impact the actual load-bearing capacity (e.g. see [32]). Finally, the quality of cast concrete near edges is generally inferior (e.g. see [31,33]), which is particularly relevant for horizontal construction joints, as present e.g. in partially prefabricated slabs.

The load-bearing capacity of keyed joints mainly depends on (i) the frictional resistance between the contact surfaces and (ii) the interlocking resistance of the keys [34] (unless adhesives are used, which is beyond the scope of this paper). The performance of an unreinforced shear key is governed by (i) its geometry (key length, depth and chamfer angle) and (ii) the concrete strength (e.g. see [35,36]). The behaviour of keyed interfaces is typically characterised by the development of a single, inclined curvilinear crack starting at the key base on its loaded side, leading to a rotation of the key (e.g. see [37]). With further loading, further diagonal shear cracks form before either the key or the corner at the loaded side of the key is sheared off [37]. Connections with several keys must fit with small tolerances to ensure (i) their combined contribution to the load-bearing capacity and (ii) the targeted alignment during erection.

2.2. Design concepts of structural connections under shear loading

Birkeland and Birkeland [23] established the *shear friction theory* to describe the frictional resistance of joints. Several researchers refined their theory to account for adhesive bond and reinforcement crossing the joint (see e.g. [26]). For construction joints with little or no reinforcement, the Mohr-Coulomb failure criterion forms the basis of most models for the shear transfer capacity v_{Rdi} of joints:

$$v_{Rdi} = c + \mu \cdot \sigma_n, \tag{1}$$

where the cohesive term c is used to characterise the adhesive bond and mechanical interlock in joints, μ is the frictional coefficient and σ_n is the stress acting perpendicular to the joint. The parameters c and μ depend on the surface roughness; experimentally fitted values are provided by design codes, incorporating a significant safety margin to respect the inherent scatter [38].

For reinforced joints, EN 1992–1-1 [34] and the *fib* Model Code 2010 [10] consider additional shear friction and reinforcement resistances with an additional additive term, which depends on the geometrical reinforcement ratio ρ, the yield strength f_y and the angle to the joint surface α of the reinforcement crossing the joint. Randl [26] proposed a refined formulation, accounting for the interaction of dowel action and tensile forces in the reinforcement.

The Mohr-Coulomb failure criterion is also commonly used as a basis for describing the load-bearing capacity of keyed joints (e.g. in EN 1992-1-1 [34] or AASHTO [39]). In this case, the term c in Equation (1) characterises the mechanical interlock provided by shear keys, while adhesion is negligible for the joint behaviour. On the other hand, Kaneko et al. [37] developed a model to describe the behaviour of unreinforced

keyed joints based on fracture mechanics, validated with tests of Bakhoum [40]. It should be noted that the design rules for keyed joints in codes ([34,39]), i.e., the experimentally fitted parameters in Eq. (1), are based on tests on keys made of concrete with aggregates considerably larger than 4 mm [17].

Regarding the geometry of keyed joints, various recommendations (established for standard concrete) are found in the literature. The AASHTO guide for the design and construction of segmental bridges [39] stipulates (i) a key depth-to-length ratio of approx. 1:2 (key length measured from mid-chamfer to mid-chamfer) and (ii) a key depth between 32 mm (1.25 in.) and twice the diameter of the largest size aggregate. EN 1992-1-1 [34] defines (i) an acceptable range for the key depth-to-length ratio of 1:3…1:10 (key length measured from beginning chamfer to end chamfer) and (ii) a minimum key depth of 5 mm. Koseki and Breen [35] suggested limiting the key depth-to-length ratio to > 1:8, mitigating the risk of crushing only one corner of the key; Specker [41] proposed a ratio > 1:6. Typically used key chamfer angles range from 18.5° (slope 1:3) [35] to 45° [42]; EN 1992-1-1 [34] suggests using an angle ≤ 30°. The angle mostly used in experimental series corresponds to 26.5° (1:2) [35,36,43].

3. Experimental programme

3.1. Overview

The effect of the key parameters for construction joints (joint surface texture) and for dry keyed joints (key geometry and number of keys) on the interface behaviour was experimentally investigated with 14 push-off tests, using the setup illustrated in Fig. 2, with the vertical load causing pure shear in the interfaces (on average); details on the loading are provided in Section 3.5. Six of the test specimens contained construction joints with and without reinforcement with varying surface roughness. The remaining eight specimens consisted of dry keyed joints with varying key geometries. Appendix A provides further information concerning the test setup. The specimen configurations are summarised in Tables 1 and 2, together with the corresponding experimental results presented in Section 4.

All specimens presented in this paper consisted of an insert of nominal dimensions 200 mm × 120 mm × 80 mm, a host piece containing the insert and a contact piece which is in contact with the insert at the tested interface (see Fig. 2). Only the inserts were produced using the *Eggshell* fabrication setup (described by Burger and Lloret-Fritschi et al. [21]); more details on the specimen production are provided in Section 3.3. The complete specimens featured a width of 300 mm, a height of 400 mm, and a thickness of 120 mm, with a nominal, tested interface measuring 200 mm × 120 mm. After production, the specimens were placed in a loading frame where the joints were horizontally compressed and loaded vertically until failure. High-resolution digital image correlation and distributed fibre optical sensing for reinforced concrete joints captured the deformations and strains on the surface and in the reinforcing bar.
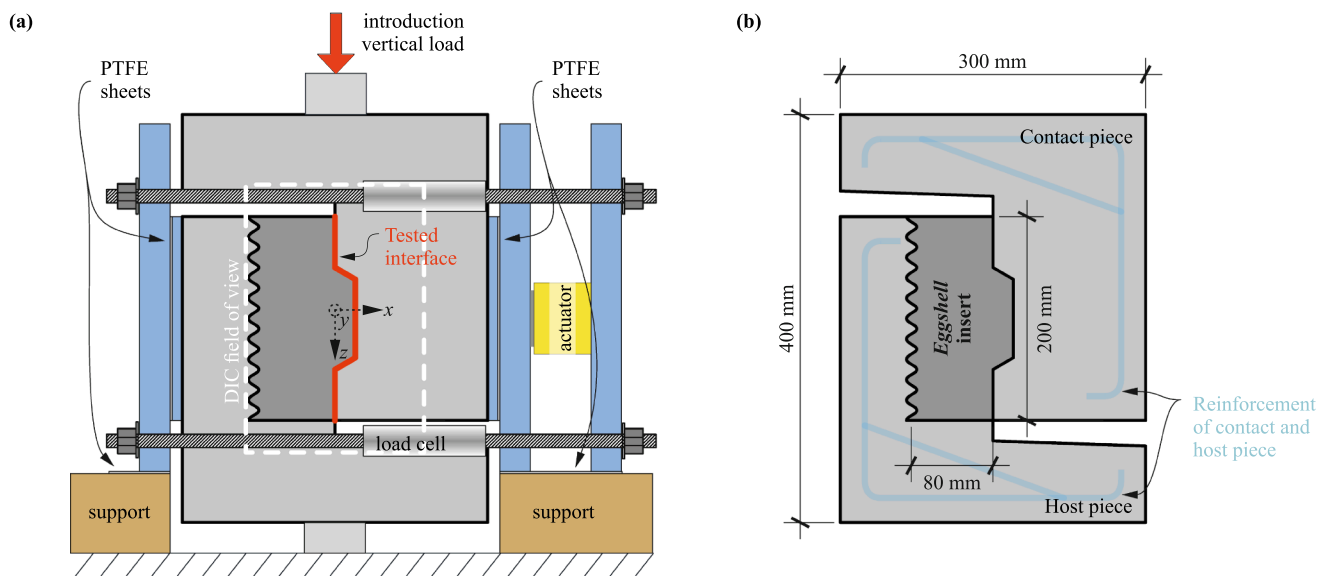

Fig. 2. Presentation of the used test setup (here for keyed joint): (a) overall information; (b) dimensions of the specimens.

Table 1
Summary of construction joint experiments (R_{td} = designed mean surface texture depth, ρ_s = reinforcement ratio, $\Delta_{x,max}$ = designed distance between top and bottom points of the surface, V_{exp} = experimentally observed shear transfer capacity, τ_{exp} = experimentally observed nominal peak shear stress, $\sigma(\Delta)$ = standard deviation of the surface imperfections, R_{td} = specimen mean surface texture depth, R_p = specimen profile roughness).

Specimen	R_{td} [mm]	Filament orientation	$\Delta_{x,max}$ [mm]	ρ_s [%]	V_{exp} [kN]	τ_{exp} [MPa]	$\sigma(\Delta)$ [mm]	R_t [mm]	R_p
EC4H	4.4	Horizontal	10	–	109	4.5	1.0	4.9	1.36
EC4HR	4.4	Horizontal	10	0.2	86	3.7	1.0	5.0	1.36
EC4V	4.4	Vertical	10	–	88	3.8	0.6	5.4	1.60
EC4VR	4.4	Vertical	10	0.2	107	4.7	0.9	5.4	1.67
EC2H	2.4	Horizontal	6	–	111	4.7	0.8	2.9	1.30
EC2HR	2.4	Horizontal	6	0.2	65	2.7	0.9	3.1	1.32

3.2. Configurations
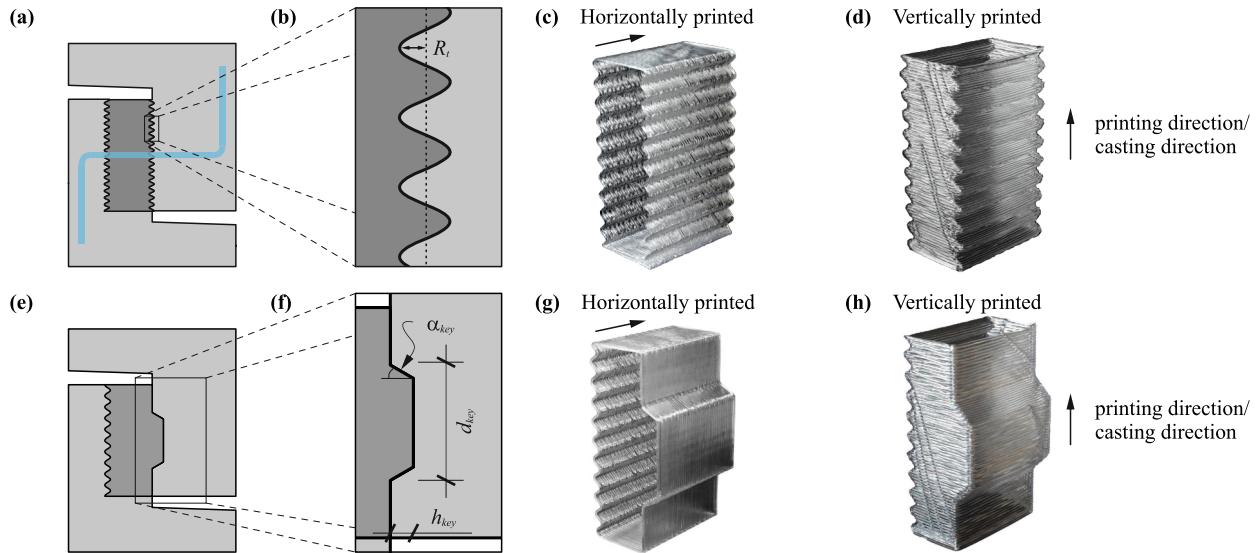
3.2.1. Construction joints

The first test series (Specimens EC) consisted of six construction joints with varying (i) joint surface corrugation and (ii) printing orientation. For each configuration, one specimen was with reinforcement crossing the joint and one without. Two types of corrugation incorporating different magnitudes of *macro*-roughness (see Section 2.1) were tested, with mean surface texture depths $R_t = \{2.4 \text{ mm and } 4.4 \text{ mm}\}$ (see Fig. 3a and b). According to EN 1992-1-1, the two texture depths represent a smooth ($R_t = 2.4$ mm) or rough interface ($R_t = 4.4$ mm). Note that the printing resolution for the formwork made even smaller surface

Table 2
Summary of dry joint experiments (α_{key} = key chamfer angle, d_{key} = key length, h_{key} = key depth, V_{exp} = experimentally observed shear transfer capacity, τ_{exp} = experimentally observed nominal peak shear stress, $\sigma(\Delta)$ = standard deviation of the surface imperfections, R_p = specimen profile roughness).

Specimen	# of keys	Filament orientation	α_{key} [°]	d_{key} [mm]	h_{key} [mm]	V_{exp} [kN]	τ_{exp} [MPa]	$\sigma(\Delta)$ [mm]	R_p
ED1H100	1	Horizontal	26.5	100	20	165	7.0	0.6	1.11
ED1V100	1	Vertical	45.0	100	20	175	7.6	0.6	1.24
ED2H50	2	Horizontal	26.5	50	10	160	6.8	0.7	1.11
ED2V50	2	Vertical	45.0	50	10	144	6.2	0.6	1.27
ED1H50	1	Horizontal	26.5	50	10	99	4.2	0.5	1.05
ED1V50	1	Vertical	45.0	50	10	93	4.0	0.5	1.19
ED1H25	1	Horizontal	26.5	25	5	74	3.2	0.6	1.02
ED1V25	1	Vertical	45.0	25	5	70	3.1	0.4	1.18

Fig. 3. Configurations of specimens: (a) and (b) construction joint with mean roughness R_t; (c) and (d) horizontally and vertically printed *Eggshell* formwork for construction joint insert (without reinforcement); (e) and (f) dry keyed joint with key geometry h_{key}, d_{key} and α_{key}; (f) and (g) horizontally and vertically printed *Eggshell* formwork for the insert.
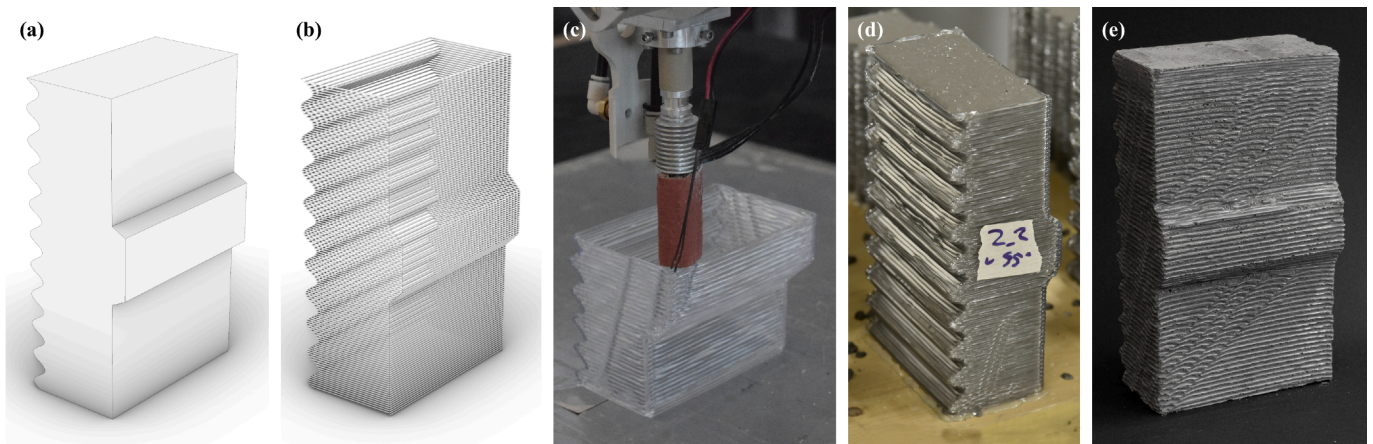
Fig. 4. Design-to-fabrication process of the inserts: (a) 3D model of the formwork, (b) formwork toolpath, (c) 3D formwork printing, (d) set-on-demand casting process, (e) concrete insert after formwork removal.
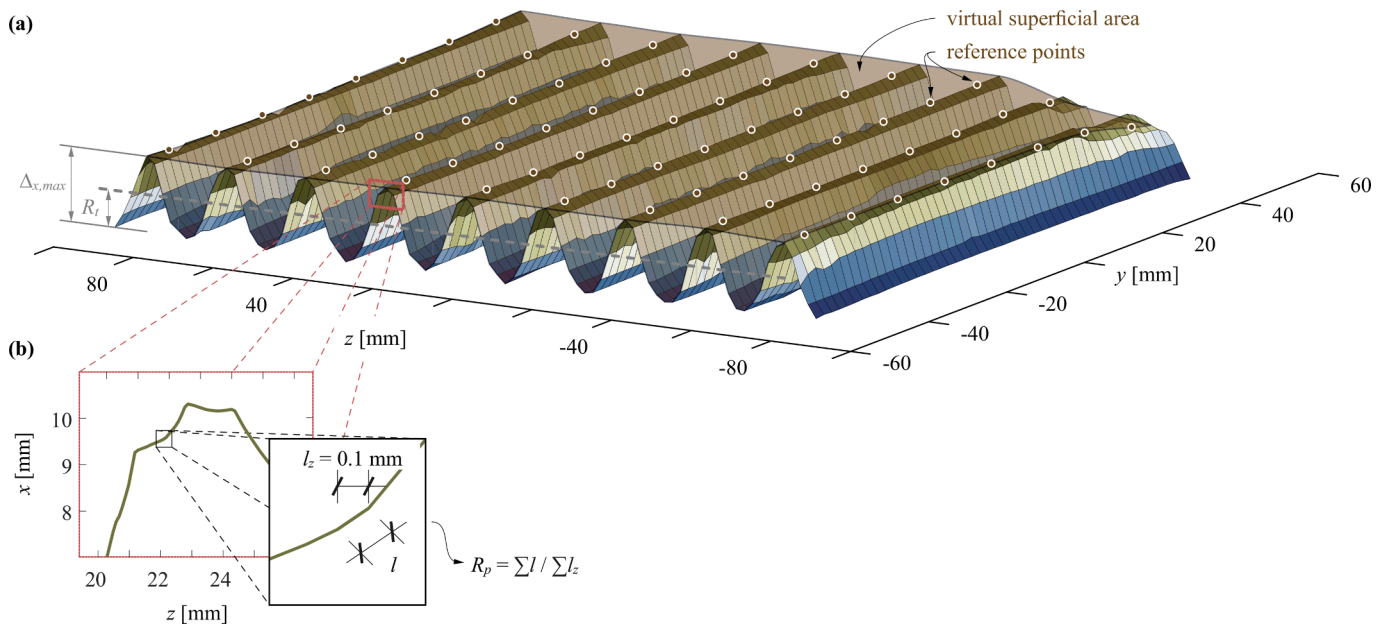
(a)

(b)

$R_p = \sum l / \sum l_z$

Fig. 5. Methods used to quantify the surface roughness (illustrated for the joint surface scan of Specimen EC4V): (a) mean surface texture depth R_t using a virtual superficial area defined by reference points and absolute value $\Delta_{x,\max}$ (note that the corrugated interface was partially damaged at y = 40 to 60 mm and z = -60 mm to -100 mm when removing the formwork); (b) profile roughness index R_p.
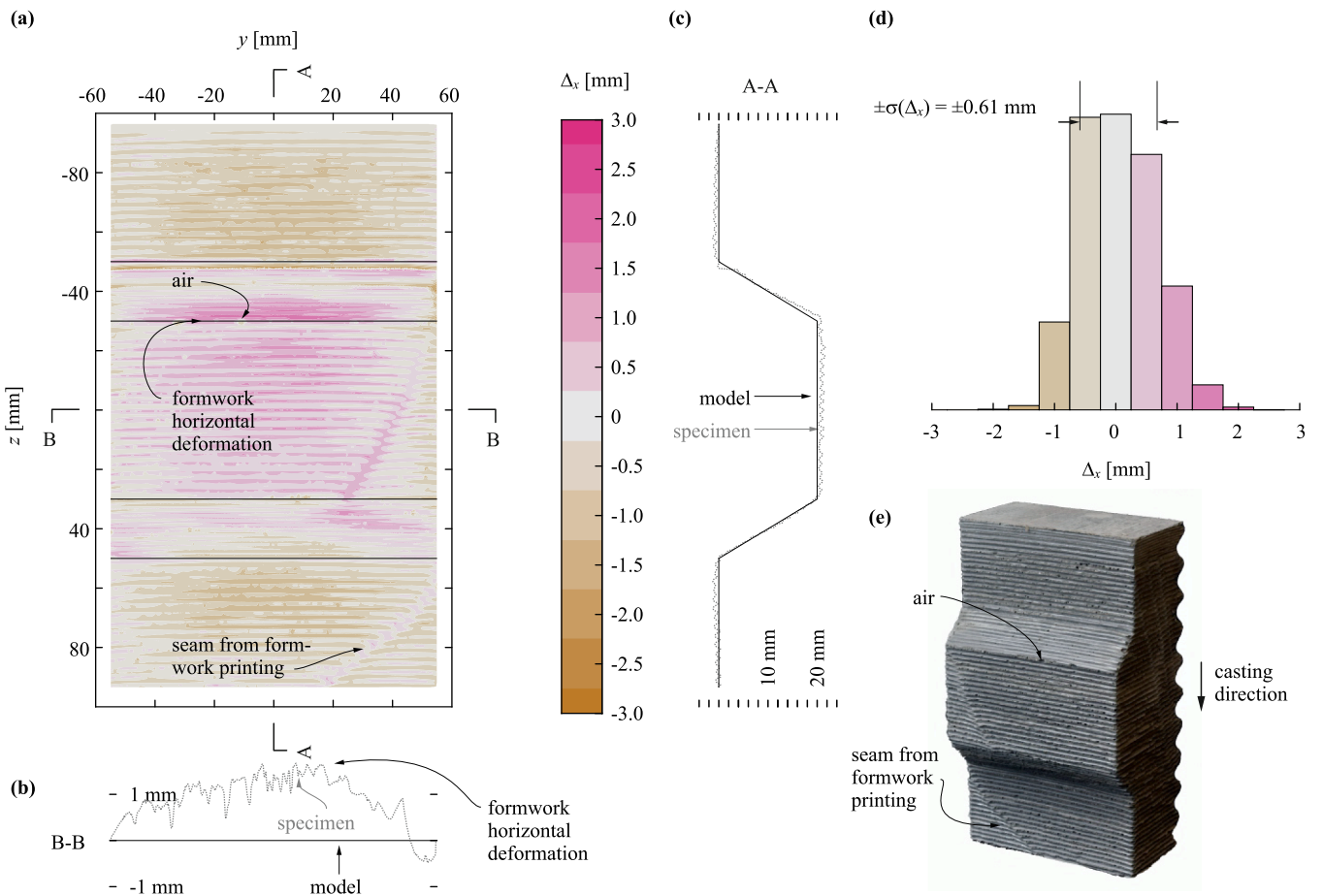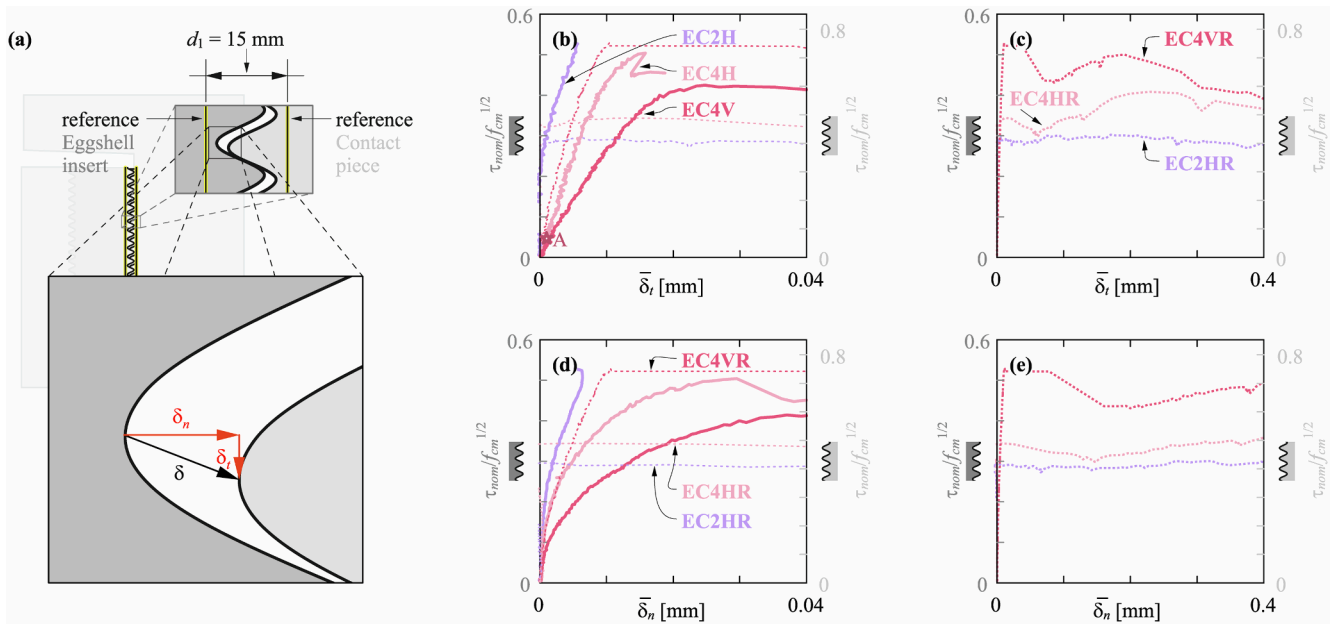

Fig. 6. Comparison of the model geometry and the scanned surface for Specimen ED1V100: (a) overall geometrical deviations Δ_x, (b) horizontal section (y-direction), (c) vertical section (z-direction), (d) histogram of deviations, (e) photo of the insert after formwork removal.

Fig. 7. Evaluation of DFC construction joints: (a) reference distance d_1 used to measure the joint deformation δ_t and δ_n; (b) and (c) normalised nominal shear stress τ_{nom} vs average joint slip $\bar{\delta}_t$; (d) and (e) normalised nominal shear stress τ_{nom} vs average joint opening $\bar{\delta}_n$. Note the different scales of the abscissas in (b), (d) and (c), (e). Left and right ordinates in the diagrams apply for τ_{nom} normalised with the square root of the concrete compressive strength of the *Eggshell* insert and the contact piece, respectively.
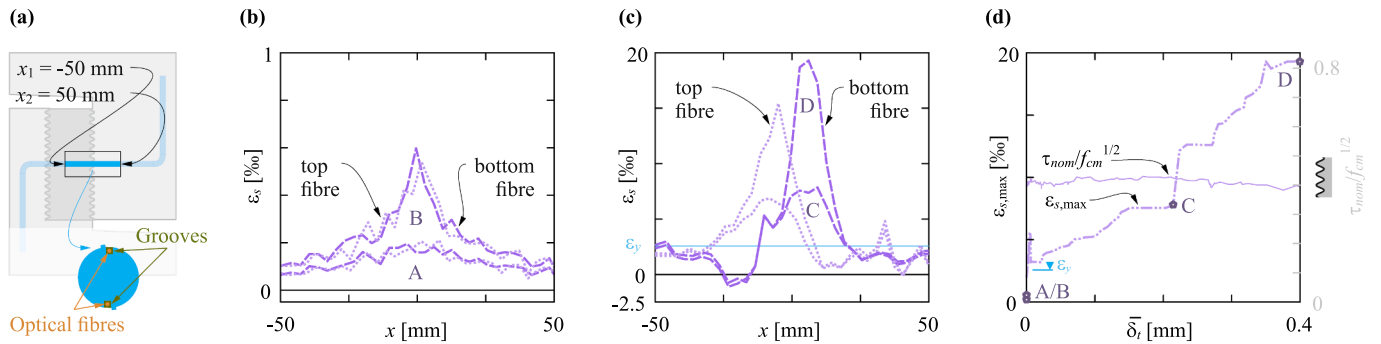
Fig. 8. Reinforcing bar strains measured with fibre optical strain sensing for Specimen EC2HR: (a) location of DFOS measurements in specimen and in cross-section of the reinforcing bar; (b) strains at the top and bottom of reinforcing bar for load steps A and B (see d) in the elastic range; (c) strains at the top and bottom for load steps C and D in the plastic range; (d) maximum strain at the joint (left ordinate) and nominal shear stress τ_{nom} normalised with $f_{cm}^{1/2}$ of the contact piece (right ordinate) vs average joint slip.
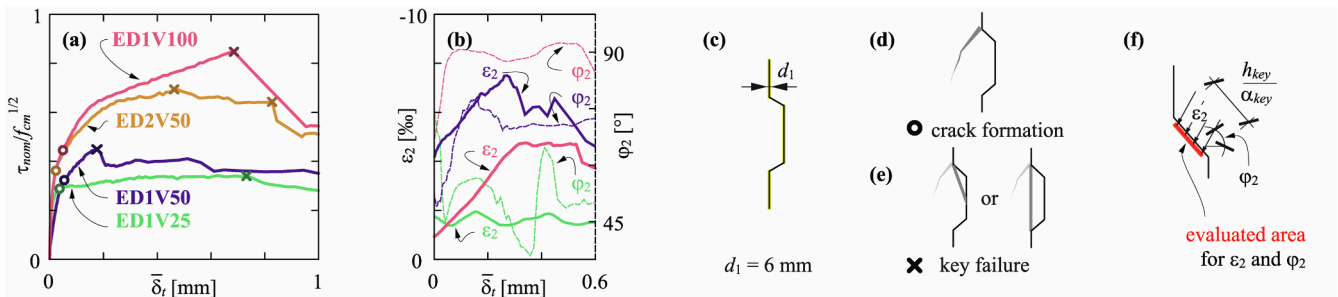
Fig. 9. Evaluation of push-off tests on DFC dry keyed joints with vertically printed formwork: (a) overview joints with ratio of nominal shear stress τ_{nom} normalised with $f_{cm}^{1/2}$ of the *Eggshell* insert against the average joint slip $\bar{\delta}_t$; (b) principal compressive strain ε_2 at the key (left ordinate) and corresponding direction φ_2 (right ordinate) against the average joint slip $\bar{\delta}_t$; (c) positions (yellow at top, middle, bottom) and reference distance d_1 used to measure the average joint slip $\bar{\delta}_t$; (d) occurrence of crack (marked with ○ in (a)); (e) key failure (marked with x); (f) evaluated area (red) for ε_2 and φ_2. (For interpretation of the references to colour in this figure legend, the reader is referred to the web version of this article.)

corrugation depths impossible. The *Eggshell*-produced formworks for the inserts were generally printed horizontally; for the higher surface texture depth R_t = 4.4 mm, companion specimens with vertically printed formwork were also tested, where the filaments caused a varying *meso*-roughness (see Section 2.1), see Fig. 3c and 3d. Arrows in Fig. 3 indicate the printing and casting direction, which always coincided. The reinforcement ratio in the specimens with reinforcement corresponded to 0.2% (one reinforcing bar ∅8 mm perpendicular to the joint plane).

In the following, the specimen configurations are designated with acronyms representing the designed surface roughness ("2″ for R_t = 2.4 mm and "4" for R_t = 4.4 mm) and the formwork printing direction ("H" = horizontal or "V" = vertical, see Fig. 3c and 3d). An "R" is attached for the specimens with reinforcement. For example, Specimen EC2HR with an *Eggshell*-produced insert (E) incorporated a construction joint (C) with a designed surface roughness of R_t = 2.4 mm with horizontal formwork layering (H) and was provided with joint reinforcement. Table 1 summarises the six construction joint configurations and the experimental results presented in Section 4.

3.2.2. Keyed joints

The second test series (Specimens ED) consisted of eight keyed joints with varying (i) number of keys, (ii) formwork printing direction (see Fig. 3) and (iii) key length d_{key} = {25, 50, 100} mm. The key depth h_{key} varied proportionally with the key length (constant ratio h_{key} / d_{key} of 1:5). The eight specimens are denominated in the following according to their configurations: e.g. Specimen ED2V50 incorporated *Eggshell*-printed (E) inserts with dry keyed joints (D), had two keys, and vertically printed formwork (V) with a key length d_{key} = 50 mm. The specimen configurations are summarised in Table 2, together with the corresponding experimental results presented in Section 4.

Note that the printing direction of the insert formworks leads to a different orientation of the filaments and different key chamfer angles of α_{key} = 26.5° (inclination 1:2) and α_{key} = 45° (1:1) in horizontal (Fig. 4g) and vertical (Fig. 3h) printing, respectively. The key chamfer angle is essential for the shear transfer capacity and the assembly of connections: smaller chamfer angles generally result in higher strength but are more challenging for assembly. The angles could be freely chosen for the horizontally printed insert formworks; hence, an inclination of 1:2, as often used in segmental construction, was selected. For the vertically printed insert formworks, producing pronounced overhangs (as required for small chamfer angles) is challenging. While overhangs up to 60° (α_{key} = 30°) have been achieved by modifying the flow rate during the print [21], and formwork stiffening ribs as employed by Burger et al. [7] could also serve to support the printing of pronounced overhangs, the chamfer angle α_{key} was chosen to 45° for the vertically printed inserts, in order to balance the geometrical tolerances and the printing speed.

3.3. Specimen production

The production of the inserts consisted of the following steps, typical for the *Eggshell* technology [21]: (i) designing the digital model of the formwork, (ii) generating the print path using COMPAS SLICER [44], (iii) 3D printing of the formwork with a thermoplastic PET-G filament of diameter 2.85 mm (nozzle diameter of 1.5 mm, print speed of 30 mm/s), (iv) set-on-demand casting and (v) removing the formwork. Fig. 4 shows the design-to-fabrication process of the inserts. Note that casting was executed after printing the entire formwork for quality control – in contrast to the application of Burger and Lloret et al. [21]. The formwork was either printed vertically or horizontally (see Section 3.2). The casting rate was 240 mm/h, pouring and stirring a batch of accelerated concrete with a height of 20 mm every 5 min; each batch was manually intermixed with the previously placed concrete to avoid cold joints between the cast layers (e.g. see [20,21]). After curing for three days at ambient conditions (approx. 20 °C), the formworks were removed using a heat gun and pliers. This process was laborious and challenging for the vertically printed formworks because the concrete interlocked with the

formwork, which slightly deformed during the casting process (see Section 4.1).

The inserts were placed inside a conventional timber formwork to produce the remainder of the specimen, i.e., the host piece and the contact piece, which were reinforced with two welded reinforcement cages with a bar diameter ∅8 mm each (Fig. 2b shows one cage per piece). The reinforced host piece was cast around the insert in a first step, such that the host piece and the insert together formed the first part of the jointed structure. Subsequently, the reinforced contact piece was cast against the insert. For the EC specimens, the resulting interface between the insert and the contact piece corresponded to typical construction joints, as illustrated in Fig. 1c-1e. In the case of keyed joints, the contact surface of the insert was impregnated with form oil before match-casting the contact piece, and the parts were separated after hardening and subsequently reassembled to represent typical keyed joints, as illustrated in Fig. 1h. Note that match-casting of the dry keyed joints was applied here to ensure successful testing of the keys without relying on production accuracy, which could have been an issue when fabricating both pieces separately with DFC, as targeted for industrial applications. With the surface accuracy achieved in this study, separate fabrication would have been possible (see Section 4).

The *Eggshell* technology has been used with larger filaments than applied for this study (e.g., see [7]), and several other DFC technologies are applicable to print reusable formworks (e.g., 3D concrete, sand or wax printing [45]). For many of these technologies, however, printing an accurate joint surface geometry, as required for fitting keyed joints, is challenging and can only be obtained with post-processing methods (e.g., milling, cutting or both).

3.4. Materials

The concrete mix used for the *Eggshell* inserts corresponded to the one used by Burger et al. [21] and Gebhard et al. [20]. As mentioned in the introduction, this mix – with a maximum aggregate size of 4 mm – is strictly speaking a mortar, but nonetheless designated as concrete here since small aggregate sizes are common in DFC. The compressive cylinder strength amounted to f_{cm} = 80.2 MPa (average of two cylinder tests), while the tensile strength was f_{ctm} = 3.2 MPa (average of two double-punch tests [46]). The Young's modulus corresponded to E_{cm} = 25 GPa (average of two cylinder tests). Note that tensile strength and the Young's modulus are distinctly lower than anticipated when applying typical design formulae based on the concrete compressive strength (e.g. according to EN 1992-1-1 [34]).

The host and the contact pieces for the specimens with construction joints were cast in concrete typical for building construction, with a maximum aggregate size of 16 mm. The compressive cylinder strength amounted to f_{cm} = 45.5 MPa (average of five cylinder tests) for the host piece and f_{cm} = 39.7 MPa (average of five cylinder tests) for the contact piece. The tensile strength corresponded to f_{ctm} = 3.4 MPa and f_{ctm} = 3.1 MPa, respectively (average of four double-punch tests for each), and the Young's modulus to 29 GPa and 30 GPa, respectively (average of three cylinder tests for each).

For the specimens with keyed joints, the host and the contact pieces were cast with ultra-high performance fibre reinforced concrete (UHPFRC), including 4% steel fibres and with a maximum aggregate size smaller than 1 mm. The UHPFRC exhibited a compressive strength of f_{cm} = 167.7 MPa (average of four cylinder tests) and a tensile strength of f_{ctm} = 13.7 MPa (average of four double-punch tests). The Young's modulus corresponded to 55 GPa (average of four cylinder tests). The use of UHPFRC ensured that failure occurred in the key (insert element).

The reinforcing bars used for the reinforced construction joints had a static and dynamic yield strength of $f_{y,stat}$ = 485 MPa and $f_{y,dyn}$ = 511 MPa, respectively, occurring at the corresponding strain ε_{sy} = 2.6‰. The tensile strength amounted to $f_{t,stat}$ = 571 MPa and $f_{y,dyn}$ = 617 MPa, respectively, occurring at the corresponding strain A_{gt} = 65‰.

3.5. Loading

Fig. 2 shows the push-off test setup used to study the performance of joints. The vertical load was monotonically increased up to the failure of the shear interface, using a displacement-controlled universal testing machine (*Schenck 1600 kN*) at ETH Zurich with a rate of 0.06 mm/min for the construction joints and 0.12 mm/min for the keyed joints. The loading rate was increased for the specimens with construction joints incorporating reinforcement after surpassing the first peak driven by adhesion and interlock (see Section 4).

An actuator (yellow in Fig. 2) and post-tensioned steel rods, both connected to heavy steel plates (blue in Fig. 2), allowed for controlling the normal stress, acting perpendicularly to the joint interface. This setup for applying the stress perpendicular to the joint was decoupled from the specimens by vertically supported steel plates and PTFE sheets, minimising any contribution of inclined rods to the shear transfer across the joint.

In the specimens with a construction joint, the normal stress perpendicular to the interface was kept approximately constant at a very low value of 0.1 MPa, as these tests aimed at representing joints with little perpendicular stress, see Fig. 1c-1e. For the specimens with dry keyed joints, a normal compressive stress of 2 MPa was applied, corresponding to a typical value for such joints (which are commonly used in prestressed segmental construction), as used in previous tests e.g. by Buyukozturk et al. [36] and Zhou et al. [43]. The normal stresses perpendicular to the joint interface exhibited only small variations, within an approximate range of ± 10% for construction joints and even lower for most keyed joints. Only specimen ED1H100 experienced a considerable reduction of the stress acting perpendicularly to the joint due to problems with the oil pump used for this specific test. Appendix A provides further information concerning the test setup and detailed data on the prevailing stress perpendicular to the joint for each specimen.

3.6. Instrumentation

Load cells were employed to measure the global vertical force (built-on load cell of testing machine) and the force perpendicular to the joints (four load cells, one per rod, see Fig. 2). The total applied load V_{exp} was divided by the total contact area to obtain the nominal shear stress τ_{nom}. 3D surface scans were performed for all joints to assess the accuracy and roughness of the joint surfaces (see Section 3.6.1). The evaluation of deformations and strains relied on high-resolution 3D digital image correlation (DIC) measurements (Section 3.6.2). Distributed fibre optical sensing (DFOS) served to evaluate the strains in the reinforcing bars used for three construction joint specimens with reinforcement crossing the joint (Section 3.6.3).

3.6.1. Surface scans

Surface scans were performed using a commercial GOM ATOS Core 300 structured light scanner. The measurement procedure consisted of (i) placing the specimens on a rotating table, (ii) defining several reference points on and in the vicinity of the specimen and (iii) using the scanner to project a pattern of light onto the surface to examine. The scanner delivered a triangulated mesh of the analysed surface with a minimum and maximum edge length corresponding to 0.129 mm and 1.548 mm, respectively. Note that the mesh spacing is automatically optimised by the software belonging to the system. It may be expected from the GOM calibration certificate that the uncertainty of the scan is approximately an order of magnitude smaller than the minimum edge length. The surface accuracy was determined by comparing the scanned mesh to a mesh of the 3D model surface (see Fig. 5a) with a grid spacing of 0.1 mm × 0.1 mm with interpolated values of the triangulated mesh.

Several methods to measure the roughness of a specific surface texture are available [30]. Typical design provisions (e.g. EN 1992-1-1 [34] or *fib* Model Code 2010 [10]) rely on the mean texture depth R_t, which correlates with an average roughness. R_t is often determined

experimentally and on-site with the so-called sand patch method [26,28], which quantifies the texture depth by means of the ratio between the volume and the projected area of fine-grained sand added to the (horizontally positioned) interface until a surface without protruding peaks is obtained. In this study, the sand patch method was applied virtually to the scanned surface of the construction joints (see Fig. 5a) using the volume below a superficial area defined by reference points on each mountain of the corrugation. The *x*-coordinates (see Fig. 2 for the coordinate system) of the reference points for this analysis were obtained by averaging the *x*-coordinates in the range of ± 6 mm in *y*-direction from each reference point. In addition to the macro-roughness quantification by the mean texture depth R_t, the profile index R_p, as first suggested by Li et al. [47], was also evaluated based on the surface scans. This index is defined as the ratio between the actual and projected surface (see Fig. 4b for a detail of the calculation) and may be considered as the specimen *meso*-roughness. Tables 1 and 2 summarise the results of both roughness quantification as well as the standard deviation of the surface accuracy $\sigma(\Delta_{x,max})$, i.e., the deviation of the built surface from the model geometry.

3.6.2. Digital image correlation

DIC is a contactless optical instrumentation technique for measuring full-field displacements on a speckled surface. A three-dimensional DIC system with high resolution was applied for this experimental exploration to capture the small deformations relevant for adhesion and mechanical interlock (see Section 2). Allied Vision Prosilica GT6600 28.8 Megapixel cameras were used with Quioptic Rodagon 80 mm lenses. The correlation was performed using the software VIC-3D from Correlated Solutions [61]. Appendix B presents additional details on the used DIC configuration.

The high-resolution DIC measurements enabled a meticulous evaluation of (i) the joint and crack kinematics and (ii) the principal strains (engineering strains) at the joint. The uncertainty of these measurements was assessed for each specimen with a zero displacement test (ZDT) before the actual test started, following the recommendations of Mata-Falcón et al. [48]. Apparent deformations observed during a ZDT (i) represent the uncertainty related to the DIC measurement and (ii) serve to determine the optimum configuration for the subset size, step size and filter size [48]. The uncertainty of the measurements for the DIC configuration chosen for this study (subset size of 21 px and step size of 6 px) was measured to be 0.33 μm (deformations) and 35 μɛ (strains) on average (see Appendix B.1 for further details on the quantification of the DIC benchmark values).

The automated crack detection and measurement approach (ACDM, [49,50]) served to determine the joint kinematics (see results in Section 4.2) based on the displacements and strains measured with DIC. The joint slip and width were evaluated continuously by assuming two rigid crack lips alongside the joint. The distance between the two reference points on each lip was set to $d_1 = 15$ mm for the construction joints (see Fig. 7a) and $d_1 = 6$ mm for the keyed joints (see Fig. 9c). The automatic positioning by ACDM of the measurement points as close as possible to crack and joint discontinuities allows reliably capturing the typically very small initial joint deformations. As further elaborated in Appendix B.2, an increase in the measurement point distance (inherent to the use of LVDTs) results in an overestimation of the joint displacements, as the measured values include concrete deformations.

The principal strains and their directions, which were used to study the local load transfer at the corrugation of construction joints and the interlocking key of keyed joints, were obtained by post-processing the DIC measurements directly at the joint in the specimens with construction joints, and below the loaded end of the key, i.e. at 2 mm distance below the joint in the specimens with keyed joints. Appendix B.3 provides further information on the procedure to obtain the high-resolution strain data.

3.6.3. Distributed fibre optical sensing

Steel strains in the reinforcing bars crossing the joint were measured quasi-continuously with standard optical glass fibres using a reflectometer capturing Rayleigh backscatter (ODiSI-6 from Luna Inc. [51]). Two glass fibres positioned at the top and the bottom of the reinforcing bar were glued with two-component commercial epoxy resin (Sikadur-52) into two straight grooves of $1 \cdot 1$ mm^2 cross-section carved along the bars (see Fig. 8a). The installation and post-processing followed the procedure described in [48,52,53].

At increasing disturbance, typical for high strains beyond the elastic limit, the load application was stopped, and a new reference measurement was taken during testing to avoid data loss. Minor disturbance of the backscatter signal was removed by applying a Hampel filter with a window size of 15 for each data point. The Hampel filter substitutes a value of concern with the median of the studied window if it deviates more than three standard deviations from the median. For some measurements, the filter was applied twice.

4. Experimental results

4.1. Description of joint surface

For digitally fabricated joints, the production accuracy decides on the applicability. For example, dry keyed joints allow for small tolerances only [54]. Hence, match-casting can only be avoided when complying with strict tolerance limits, in the range of a few millimetres at most. For construction joints, the design according to pertinent design codes (e.g. EN 1992-1-1 [34]) relies on the joint surface roughness (see Section 2), and the actual local accuracy is less critical.

Fig. 6 compares the surface scan with the model geometry for the *Eggshell* insert of Specimen ED1V100. Fig. 6a illustrates the geometrical deviations Δ_x of the joint surface, while Fig. 6b and 6c show sections at $z = 0$ and $y = 0$, respectively. Fig. 6d provides the histogram of all data points for Δ_x shown in Fig. 6a with the corresponding standard deviation, while Fig. 6e shows a photo of the scanned insert under consideration. The deviations Δ_x combine printing defects, deformations originating from casting the inserts and defects generated when removing the formwork. Fig. 6a and 6b evidence that the formwork bulged slightly at the centre due to the hydrostatic pressure during casting (bulging of approximately 1 mm). Further, Fig. 6c shows an artefact resulting from the 'seam' (the transition from one 3D printed layer to the following layer) in the formwork; note that this artefact was present in the joint surface of all vertically printed dry keyed joints. Finally, the surface scans identified air entrapped in the formwork (e.g. see Fig. 6a at $y = -10$ mm and $z = -30$ mm). Appendix C.1 provides surface scan comparisons for construction joint specimens.

Tables 1 and 2 summarise the geometrical deviation for all specimens: the standard deviation $\sigma(\Delta_x)$ of the deviations between the scan and the model geometry shows that the specimens produced with a vertically printed formwork had a higher accuracy than the specimens with a horizontally printed formwork (see EC2H and EC4H compared to EC4V as well as ED1H25 compared to ED1V25), despite the challenges of printing the formwork with overhangs (see Section 3.3). The reason is primarily the deformation of the formwork occurring during casting, given the lower stiffness of the horizontally printed formworks with longer spans from edge to edge (see "casting direction" in Fig. 2).

Concerning the surface roughness, the actual values of the mean texture depth R_t for the construction joints (see R_t in Table 1) were slightly higher than intended (R_{td}, see Section 3.2). This deviation occurred most likely due to deformations of the formwork while casting and local deficiencies from printing and removing the formwork. Specimens produced with vertically printed formwork generally exhibited a higher *meso*-roughness than specimens relying on horizontally printed formwork (see R_p index in Tables 1 and 2). The reasons are (i) the regular fine corrugation induced by the process of printing the plastic formwork and (ii) the defects resulting from removing the formwork of the inserts, which was more challenging for vertically printed formwork.

4.2. Load-deformation behaviour

This subsection compiles the experimental results relevant to discuss the performance of digitally fabricated joints. The maximum applied load V_{exp} and the resulting shear stress τ_{exp} are summarised in Tables 1 and 2. Further detailed evaluations are presented in Appendix C.2.

4.2.1. Construction joints

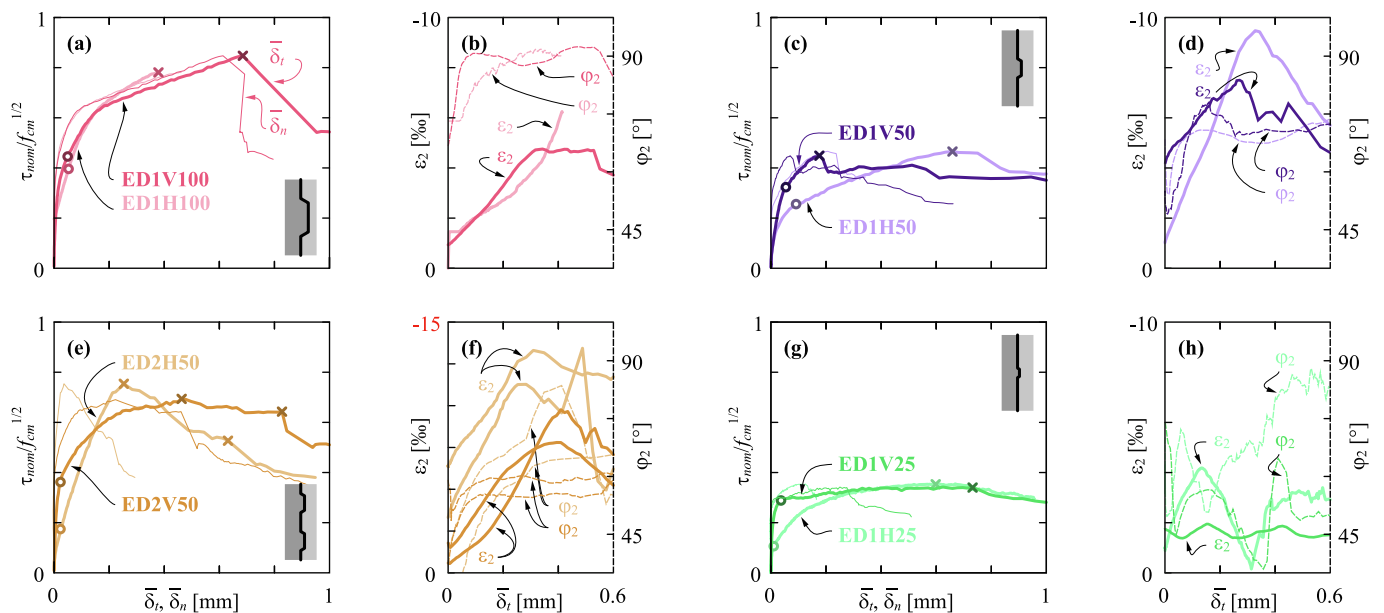Fig. 7 illustrates the load-deformation behaviour of the DFC

Fig. 10. Evaluation of all push-off tests on DFC dry keyed joints: (a, c, e, g) ratio of nominal shear stress τ_{nom} normalised with $f_{cm}^{1/2}$ of the *Eggshell* insert against the average joint slip $\bar{\delta}_t$ and opening $\bar{\delta}_n$; (b, d, f, h) principal compressive strain ε_2 at the key (left ordinate) and corresponding direction φ_2 (right ordinate) against the average joint slip $\bar{\delta}_t$.
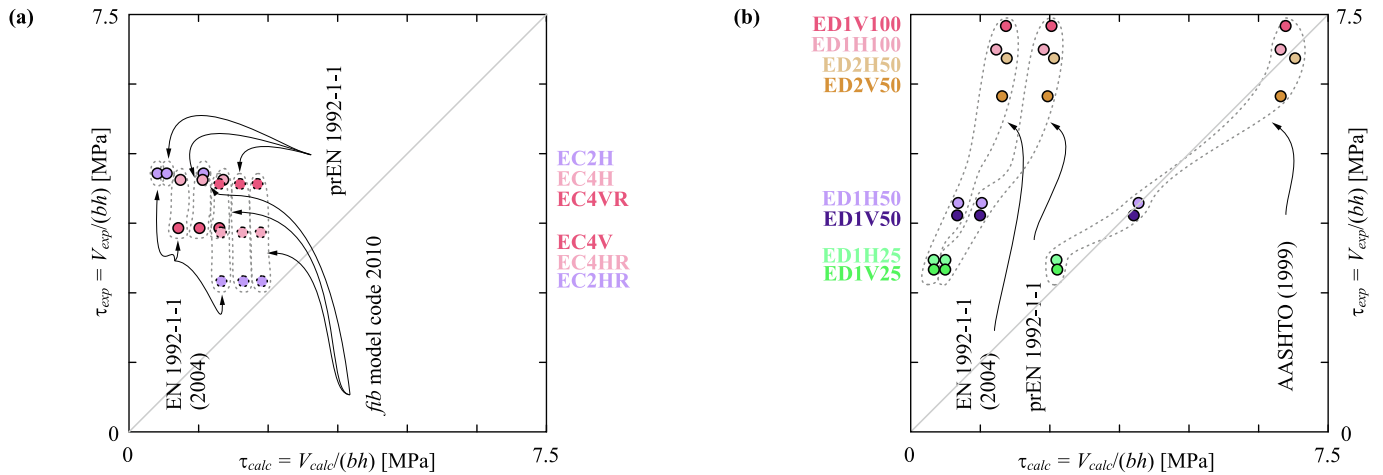
Fig. 11. Comparison of predicted and observed shear transfer capacity of all specimens: (a) construction joints and (b) dry keyed joints. Note that the predicted values rely on the mean concrete compressive strength f_{cm} of (a) the contact piece and (b) the *Eggshell* insert.

construction joints. The joint slip δ_t and opening δ_n were evaluated continuously along the joint (Fig. 7a). Fig. 7b to 7e show the nominal shear stress τ_{nom} – normalised with the square root of concrete compressive strength (in MPa) of the *Eggshell* insert (left ordinates) and of the contact piece (right ordinates) – against the average joint slip $\bar{\delta}_t$ (Fig. 7b and 7d) and the average joint opening $\bar{\delta}_n$ (Fig. 7b to 7e). Solid and dashed lines are used for the specimens without reinforcement and with reinforcement crossing the joint, respectively. The different scale of the abscissa facilitates plotting the response of the specimens without reinforcement, exhibiting very small deformations at failure (Fig. 7b and 7d) and with reinforcement, exhibiting larger displacements (Fig. 7c and 7e).

Appendix C provides further results of the high-resolution instrumentation. For example, the local measurements show that the joint slip δ_t is approximately constant over the joint length, while the joint opening δ_n is largest at the middle of the joint and smallest at the edges. The load transfer is thus more pronounced at the edges with the minimum joint opening (e.g. [26]). Note that δ_n was also larger in the middle of the joint for reinforced construction joints at small displacements, i.e., as long as the shear transfer capacity was mainly governed by adhesion and interlock.

All construction joints failed through the teeth of the corrugation affecting both used materials (*Eggshell* insert and contact piece, see Section 3.4), independent of the mean texture depth (see pictures of the failed joint in Fig. C.6 and Fig. C.7). Note that despite the higher compressive strength of the *Eggshell* inserts concrete, both materials provide a similar tensile strength (see Section 3.4); hence, a similar shear transfer capacity could be expected. As the teeth failed, the differences in the mean texture depth R_t, e.g. between Specimen EC2H and EC4H, did not affect the shear transfer capacity, which was reached at an average joint slip $\bar{\delta}_t$ of 6 to 20 μm (see Fig. 7b and 7d). Fig. 7d suggests that the stiffness of Specimen EC2H was higher than that of Specimen EC4H, given the clearly smaller joint opening, possibly caused by slightly deformed joint surfaces or slightly different angles of the corrugation. However, it should be noted that the captured slips and joint openings are in the magnitude of measurement uncertainty; hence, drawing definitive conclusions is questionable.

Specimen EC2H with $R_t = 2.9$ mm had a higher shear transfer capacity than Specimen EC4V with $R_t = 5.4$ mm. On the other hand, Specimen EC2HR had a lower shear transfer capacity than Specimen EC4VR (over the complete slip range, see thin dashed lines in Fig. 7b for small slip). These results show that the scatter is considerable concerning both the stiffness and the shear transfer capacity when adhesion and interlock are governing the behaviour (i.e. in the range of approximately $0 < \bar{\delta}_t < 10$ μm).

Fig. 8 shows the strains measured with DFOS at the top and bottom of the reinforcing bar crossing the joint of Specimen EC2HR. The results indicate that the bar (i) is active as soon as the joint is loaded and (ii) starts yielding (see reinforcement yield strain ε_y in Fig. 8c and 8d) before the full shear transfer capacity from adhesion and mechanical interlock is mobilised (at $\bar{\delta}_t$ slightly above zero in Fig. 8d). Initially (steps A and B), the bar is mainly loaded in tension, before dowel action (i.e., bending of reinforcing bar) continuously increases (C and D), as the horizontal shift of the maximum strains and the increasing strain difference between top and bottom fibre in load steps C and D indicate.

Thanks to the reinforcement, which provides lateral restraint to the joint opening causing compressive stresses hence increasing friction in the joint (already at small joint slip) and dowel action (at larger joint slip), a significant amount of the joint shear transfer capacity is maintained until large joint slips. The combination of both effects likely caused the second increase of resistance of Specimen EC4VR after surpassing the first peak resistance (see Fig. 7c), given the distinctly higher roughness of Specimen EC4VR (see Table 1).

4.2.2. Keyed joints

Figs. 9 and 10 illustrate the behaviour of the specimens with dry keyed joints. Fig. 8a compares the load-deformation behaviour of the vertically cast specimens by plotting the nominal (vertical) shear stress τ_{nom}, normalised with $f_{cm}^{1/2}$ (of the *Eggshell* insert since the failures were triggered at the shear key) against the average joint slip $\bar{\delta}_t$ and opening $\bar{\delta}_n$. Fig. 9b shows the principal compressive strains ε_2 (solid lines) and their direction φ_2 (dashed lines) at the chamfer of the shear key (see Fig. 9f), respectively, against the average crack slip $\bar{\delta}_t$. Fig. 9c-9f illustrate the key geometry, the observed crack and failure patterns, as well as the evaluation of principal strains and their direction. Fig. 10 compares the behaviour of the four pairs of companion specimens, differing only in the printing and casting directions (vertical or horizontal), using the same representations as in Fig. 9a and 9b.

The $\tau_{nom} - \bar{\delta}_t$ curves in all dry keyed specimens exhibit three distinct phases: In the first phase, the frictional resistance and the mechanical interlock gradually increase (see increasing φ_2 in Fig. 9b). The second phase initiates after an inclined crack (as illustrated in Fig. 9d) opens at the edge of the loaded end of the key, which is denoted with the marker ○ in Figs. 9 and 10. In this second phase, the interlocking key governs the overall shear transfer; the principal compressive strain direction reorients towards the direction of the load introduction (e.g. $\varphi_2 = 75°…90°$ in Fig. 9b for Specimens ED1V100 and ED1V50) when the key is activated. After the formation of several cracks along the key, it shears off (see Fig. 9e, denoted with the marker × in Figs. 9 and 10), either partially (ED1V25 and one key of ED2V50) or completely (all other

specimens). Beyond the key failure, in the third phase, the applied load corresponds to the residual frictional resistance of the joint, continuously decreasing with increasing joint slip. This observed behaviour was previously described by other researchers based on experimental evidence and/or modelling of conventionally fabricated keyed joints (e.g. see [35–37,43,55]).

As seen from Fig. 10, the initial stiffness of joints with vertically printed formwork was markedly higher than that of joints with horizontally printed formwork, most probably due to the higher profile roughness R_p originating from the formwork filament direction (see Table 2). On the other hand, the shear transfer capacity of horizontally printed joints was generally slightly higher, probably owing to their smaller key chamfer angles. Note that for ED1H100, the stress perpendicular to the joint could not be kept constant, and the measurement system stopped prematurely (see details in Appendix A). The key chamfer angle also entailed the inferiority of the average joint opening $\bar{\delta}_n$ for horizontally printed joints than for vertically printed joints.

The frictional resistance controlled the load-bearing capacity of Specimen ED1V25, which combined the smallest key dimension ($d_{key} = 25$ mm, i.e. a key depth of merely 5 mm, i.e., roughly 1.25 times the maximum aggregate size), and the larger key chamfer angle of 45°. This key did hardly contribute to the overall load-bearing capacity (see the quasi-constant value of ε_2 in Fig. 10h). The keyed joints with larger height (and depth) exhibited an increasing interlocking effect with increasing key dimensions (+25% shear transfer capacity with $d_{key} = 50$ mm and + 150% with $d_{key} = 100$ mm, both compared to $d_{key} = 25$ mm). The peak compressive strain at the key reached 8‰…14‰ for the specimens with fully interlocking key (e.g. see ED1H50 and ED2H50 in Fig. 10f). The specimens with two keys (ED2V50 and ED2H50) underwent progressive failure, i.e. the two keys failed one after the other, with both keys clearly activated (see the decrease of shear transfer capacity in Fig. 10e after reaching the shear transfer capacity); however, the shear transfer capacity for Specimen ED2V50 with the vertically printed formwork was clearly lower than that of the specimens with one key and twice the height and depth (ED1V100) because one key of Specimen ED2V50 sheared off only partially.

5. Discussion

DFC provides new opportunities to produce load-bearing joints. In traditional construction, the performance of joints depends on the execution quality, and their production is labour-intensive. Thanks to its geometrical flexibility, DFC enables (i) the fabrication of controlled joint surface textures, (ii) the high and controlled fabrication accuracy and (iii) the fabrication of individual configurations (e.g. placing reinforcement crossing the joint, varying configuration of keys) without significantly increasing production efforts.

The presented experimental exploration proved that the used *Eggshell* technology allows fabricating the joint surface roughness according to a specific design. The roughness may be controlled via (i) the printed shape and (ii) the direction of the printed filament. Such an approach would also apply to other DFC technologies, such as 3D concrete printing, to print formworks, structures, members or parts thereof. These topics are currently part of various research efforts (e.g. [56]).

The *Eggshell* technology demonstrated to ease the production of the formwork for conventional reinforced construction joints. However, the placement of continuous reinforcing bars or meshes crossing an additively printed surface requires good coordination of the printing process and the reinforcement placement. Burger et al. [7] proved the feasibility of this concept for a real-scale application.

The evaluation of the 3D surface scans demonstrated that DFC enables producing joints with high accuracy, which is essential for fitting keyed joints without having to recur to expensive match casting. The surface of the keyed joints in this study, fabricated with the *Eggshell* technology, coincided well with the designed model surface, with a standard deviation between 0.4 mm and 0.7 mm and maximum

deviations of approximately 2 mm, depending on (i) the formwork geometry, whose accuracy is controlled by the printing setup, (ii) the formwork deformations occurring during casting, which are controlled by the formwork stiffness and the casting process, and (iii) deficiencies originating from the formwork removal. All these decisive factors for geometrical deviations could be further optimised, e.g. by providing stiffening ribs for the formwork [7] or by facilitating the formwork removal. Regarding the latter, an option for the formwork removal could be to use a formwork material which would melt at low temperatures to combine removing the formwork and steam-curing. However, it must be noted that printing a geometrically accurate formwork for a joint of a precast element with typical dimensions of several meters in length and a few meters in (transportable) width would be more challenging than printing the formwork of the small insert used for the presented exploration and requires further testing.

In addition to the fabricability and performance of the joints, design codes must provide reliable predictions to achieve acceptance of digital fabrication in the construction industry. Besides potential differences due to the fabrication process, the use of concrete mixes with very small aggregates (typically below 4 mm) questions the application of design code provisions calibrated on joint experiments using common concrete with larger aggregate sizes. To examine the applicability of existing design codes to digitally fabricated joints, Fig. 11 compares the experimentally observed nominal peak shear stress ($\tau_{exp} = V_{exp}/(bh)$ see Tables 1 and 2) of all joints to their shear transfer capacity, τ_{calc}, predicted based on (i) the current EN 1992-1-1 (Clause 6.2.5) [34], (ii) the revised prEN 1992–1-1 prepared for the formal vote (Clause 8.2.6) [57], (iii) the *fib* Model Code 2010 (Section 6.3) [10,26] and (iv) the AASTHO guide specifications for the design and construction of segmental concrete bridges (Clause 12.2.21) [39]. The experimentally fitted parameters c and μ from Equation (1) were used according to the corresponding design code. Furthermore, the predictions rely on the average concrete compressive strength f_{cm}, (see Section 3.4), the effective force acting perpendicularly to the joint at the peak load and the measured surface roughness of each specimen.

As Fig. 11a shows, all construction joints, without and with reinforcement, exhibited a higher shear transfer capacity than the design values predicted by the current and revised EN 1992-1-1 [34,57] as well the *fib* Model Code 2010, despite using concrete with small aggregates. However, the behaviour of the six joints was subjected to considerable scatter despite the strict control of the material properties and of the geomety of the inserts and their surface texture. As evaluated by Figueira et al. [38], the effective resistance factor (mean experimentally observed strength divided by its design value) is considerably higher for rough than smooth surfaces in construction joints subjected to shear loading designed according to EN 1992-1-1 [34] (rough: μ = 2.52, σ = 0.803; smooth: μ = 1.37, σ = 0.064). Compared to these values, the scatter observed in the DFC joints related to the joint surface texture and the material is not clearly smaller. However, the superior geometrical control achieved in production with DFC allows for designing the required roughness of construction joints more accurately than with traditional construction methods.

Fig. 11b indicates that EN 1992-1-1 [34,57] heavily underestimates the load-bearing capacity of dry keyed joints, while the AASTHO design code [39] predicts the capacity rather accurately regardless of the geometry and number of keys. While the background of the design provisions of EN 1992-1-1 [34,57] is not documented to the authors' knowledge, the AASTHO design code [39] relies on experimentally fitted parameters, which apparently also apply to the tested configurations, despite the use of concrete with a maximum aggregate size of 4 mm.

6. Summary

Connections are essential for the load-bearing capacity of concrete structures, particularly when using digital fabrication with concrete

(DFC); relatively small elements with many joints having to transfer significant load often result when using DFC to produce structural members with complex shapes. On the other hand, DFC allows producing bespoke geometries and surface roughness. Accordingly, it offers new opportunities for designing concrete connections between adjacent members or parts thereof.

This paper discusses the design, fabrication and structural testing of digitally fabricated joints using the DFC technology *Eggshell* to 3D print the formwork for joint surfaces. The experimental campaign included construction joints with and without reinforcement and with varying joint surface texture to control the roughness, as well as digitally fabricated keyed joints with varying dimensions in height, depth and key chamfer angle relevant for prefabricated building construction. The construction joints and dry keyed joints were produced using concrete with aggregates of 0...4 mm size typically applied in DFC.

3D surface scans provided detailed feedback on the geometrical accuracy of the produced joints compared to the model geometry. The accuracy depended on the geometry and stiffness of the printed formwork as well as the casting and formwork removal process. For the *Eggshell* elements of 200 mm × 120 mm × 80 mm produced in this study, a high accuracy with deviations from the target geometry below 2 mm could be achieved (standard deviation between 0.4 mm and 0.7 mm for keyed joints). However, the accuracy may require further improvement when producing real-scale reinforced concrete elements.

The joints were tested using a push-off setup to assess their interface shear transfer capacity. High-resolution instrumentation (digital image correlation and fibre optical sensing) (i) captured the joint kinematics in the required order of magnitude of a few micrometres, (ii) enabled an in-depth study of the load transfer at the corrugation over the height of construction joints and (iii) allowed discussing the efficiency of varying key dimensions. Such detailed information may foster a further understanding of the behaviour of joints loaded in shear, given the high dependency of design concepts on experimentally fitted results. Overall, the tests showed that all digitally fabricated joints met or outperformed requirements defined in pertinent design codes.

The presented experimental exploration concentrated on joints subjected to pure shear loading and relied on small aggregate concrete. However, typically joints resist combined loading, which would require further examination, e.g. for shear loading combined with imposed strain gradients. The combined use of surface scanning, high-resolution DIC and DFOS, applied in the presented exploration, may foster a further understanding of the behaviour of relevant joint configurations, aiming at reducing the number of tests required for validation. Finally, future research with DFC should address the fabrication of matching keys for large-scale elements to avoid the match-casting process, which limits the number of elements cast per day.

7. Data availability statement

The data that support the findings of this exploration are openly available in ETH Research Collection at https://doi.org/10.3929/ethz-b-000565785.
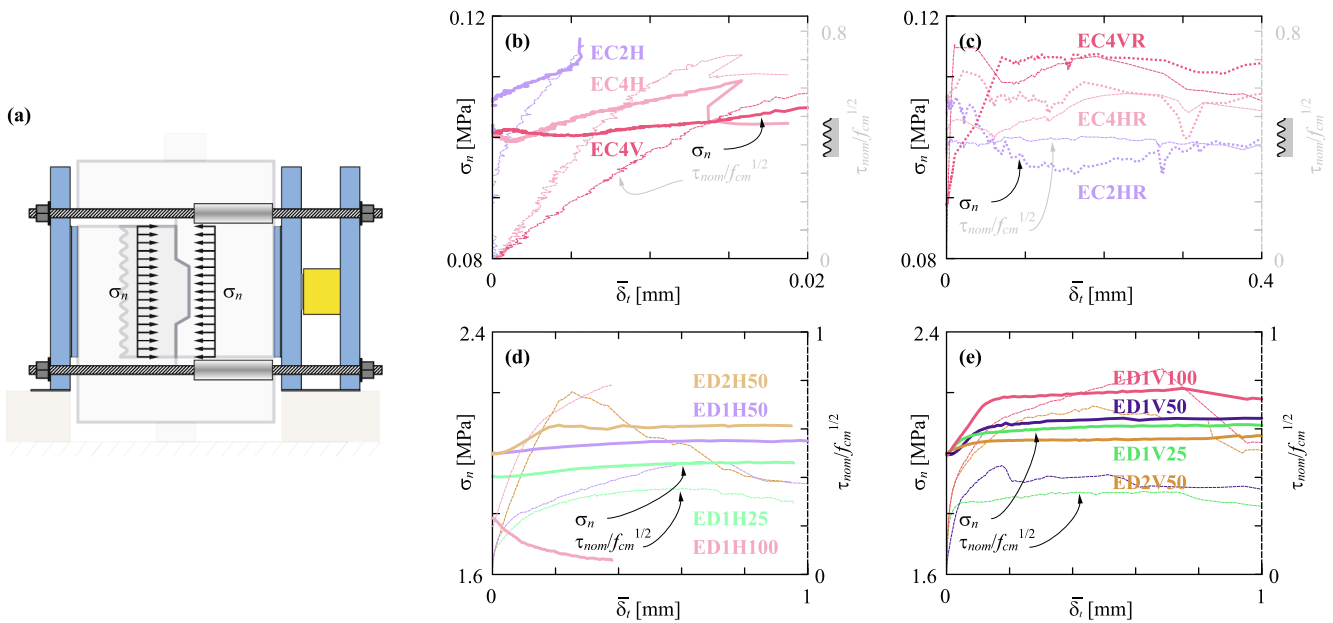
Declaration of Competing Interest

The authors declare that they have no known competing financial interests or personal relationships that could have appeared to influence the work reported in this paper.

Data availability

The data that support the findings of this exploration are openly available in ETH Research Collection at https://doi.org/10.3929/ethz-b-000565785

Appendix A

Validation of used test setup

Many experimental campaigns have been dedicated in the past to the investigation of the shear transfer across jointed or cracked interfaces. Several reviews of these campaigns using various test setups are available in the literature (e.g. [29,58–60]). Testing joints or cracks under shear loading is challenging (e.g. see [26,59,61]): Even a just slightly eccentric load introduction or external clamping forces may lead to uncontrolled tensile and compressive stresses perpendicular to the shear interface, leading to inhomogeneous shear stress distributions as particularly the frictional contribution to the shear transfer capacity strongly depends on the normal stress perpendicular to the shear interface.

The used Z-type push-off test setup initially aims at a perfect alignment of the applied load and the shear interface. However, unless the deformations perpendicular to the shear interface are fully restrained – which is hardly possible in reality –, an eccentricity will occur during the test as soon as the joint opens, resulting in relative translations and rotations of the specimen halves. The opening of the joint may be restrained by internal reinforcement, external (often prestressed) rods or actuators. In some push-off test configurations, rods incline during the test and contribute to the overall shear transfer capacity (e.g. see [61]). Accordingly, the comparison of results obtained with specimens tested under varying boundary conditions prevailing perpendicularly to the interface is not straightforward, given the influence of the typically very small joint opening on the load-deformation behaviour and strength (e.g. see [58,59]).

In the experimental campaign presented in this paper, the variation of the load acting perpendicularly to the joint remained within ± 10% during the test (see Fig. A1), except for Specimen ED1H100, in which the oil pressure decreased while testing. Fig. A2 shows the ratio of the force parallel and the force perpendicular to the joint against the average joint slip $\bar{\delta}_t$ for the specimens with keyed joints to exemplify the influence of the stress acting perpendicularly to the joint on the actual joint shear transfer capacity. Fig. A2a indicates that the shear transfer capacity of Specimen ED1H100 could

Fig. A1. Stress acting perpendicularly to the joint: (a) setup to apply load perpendicular to the joint; (b)-(e) nominal stress perpendicular to the joint σ_h (left) and nominal shear stress τ_{nom} normalised with $f_{cm}^{1/2}$ of contact piece (right) against the average joint slip $\bar{\delta}_t$ for (b) unreinforced construction joints, (c) reinforced construction joints, (d) and (e) for dry keyed joints.
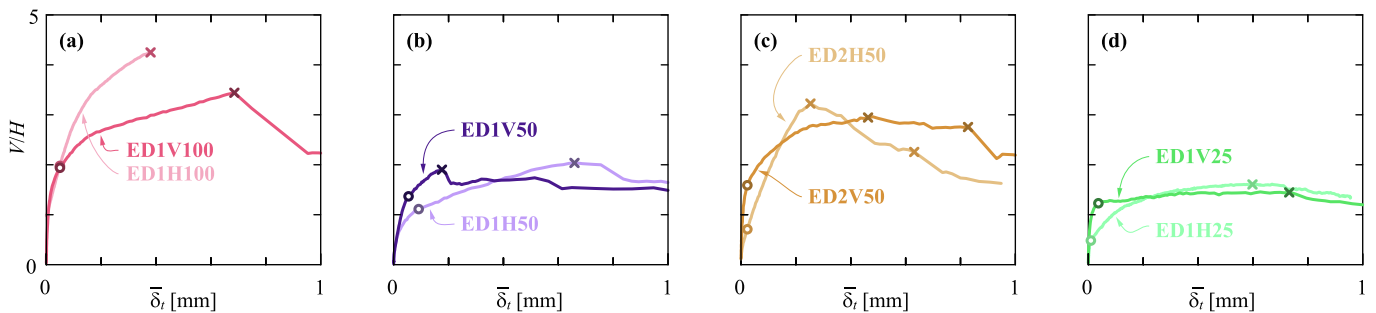
Fig. A2. Stress acting perpendicularly to the joint: (a)-(d) ratio of forces applied parallel and perpendicular to the joint against the average joint slip $\bar{\delta}_t$.
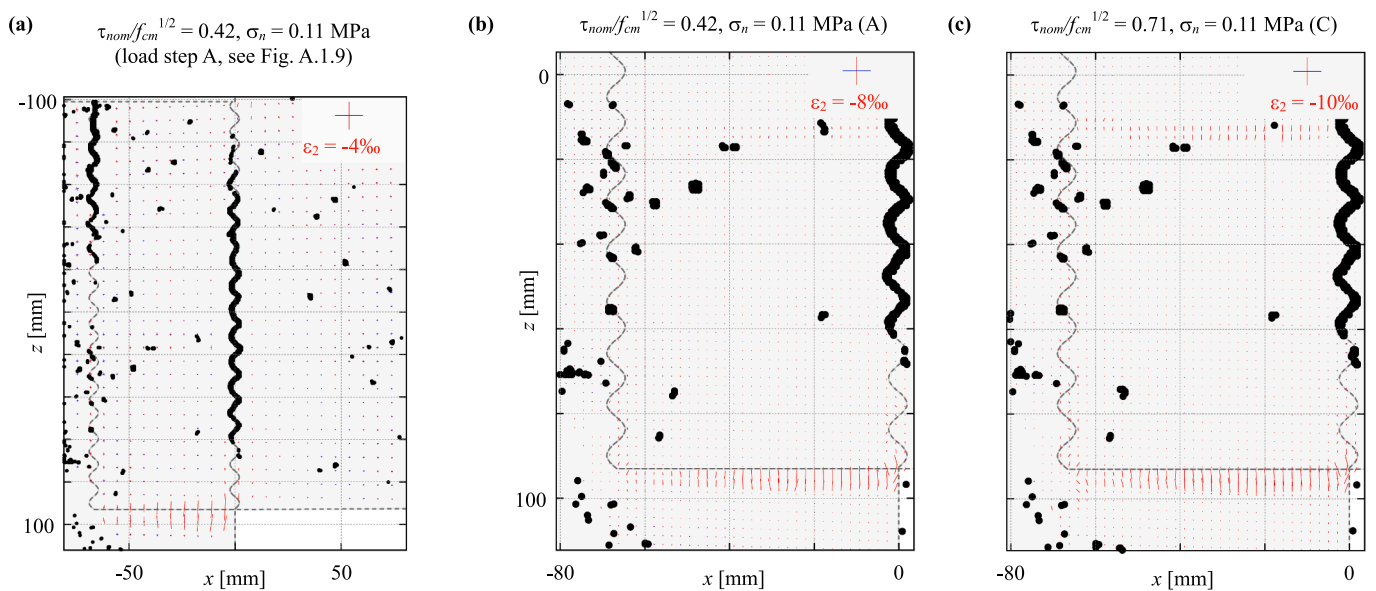
Fig. A3. Orientation and magnitude of principal strains ε_1 and ε_2 determined from high-resolution full-field displacements with DIC measurements for Specimen EC2H for two load steps: (a) load step A with $\sigma_v/f_{cm}^{1/2} = 0.42$ with data averaging over 11 mm (filter size 45); (b) load step A with data averaging over 3.5 mm (filter size 15); (c) load step C with data averaging over 3.5 mm (filter size 15). The black hatch indicates the locations with unrealistically high tensile strains (see Appendix B.3). The relevant section of the test setup (*Eggshell* insert, host and contact piece) is provided in the background with grey lines. Note that the scale of ε_1 and ε_2 is adjusted from (a) to (c) (see legend in each figure).

have been superior to ED1V100 with equivalent stress perpendicular to the joint.

Results of the high-resolution instrumentation with DIC revealed that the strains of the push-off specimens differed from the values expected e.g. based on a linear elastic finite element analysis. Fig. A3 illustrates the magnitude and orientation of the principal strains, highlighting that (i) the joint between the insert and the host piece (opposite to the tested joint) opened and (ii) very high compressive strains occurred locally at the bottom and in the lower half of the joint (see concentrated red lines). These local kinematics and strain distributions must originate from the overall behaviour of the push-off test setup when loaded. However, the field of view captured with DIC was limited to the close vicinity of the joint (see Fig. 3). Furthermore, these local effects seemingly did not influence the behaviour of the actually tested joint (see Fig. C6b, Fig. C7b and Fig. C8). Therefore, this paper refrains from further discussing these observations.

Appendix B. 3D digital image correlation details

B.1. Measurement uncertainy

Two "Allied Vision Prosilica GT6600" monochrome cameras (28.8 Megapixel, 36×24 mm sensor) were used, positioned with a baseline length of 245 mm at a distance of 600 mm to the specimen surface, leading to a stereo angle of $21°$. Employing Rodagon 80 lenses, the field of view amounted to approximately 255 mm $\times$ 170 mm (see Fig. 3), resulting in a captured resolution of 0.04 mm/px. The speckles applied to the white-painted specimen surface had a nominal diameter of 0.18 mm. DIC measurements were captured at an interval of 2 Hz. The correlation was conducted with the software VIC-3D from Correlated Solutions [62].

The measurement uncertainty was evaluated for each specimen with a zero displacement test (ZDT). Fig. B1a shows the measured in-plane deformation for the ZDT of Specimen ED1V100, which is representative of the other specimens. The 6x18 quadratic cells shown in Fig. B1a present the averaged deformations within the considered subarea each. The subdivision of the area of interest at the considered joint into cells follows the recommendations of VDI 2626 [48,63]. The selected subset and step size amount to 21 px and 6 px, respectively. The *NV*-value (=average of all cell values according to VDI 2626 [48,63]) results in 0.33 μm, which may be considered as an estimator of the measurement uncertainty. Fig. B1b provides the evolution of the standard deviation of the measurement uncertainty for in-plane displacements of all cells, $\sigma(dx_q)$ and $\sigma(dz_q)$, with the maximum, mean and minimum values depending on the subset size (values of all cells shown in the histogram). The value of the subset size was chosen close to the point where the curve becomes approximately asymptotic.

The results of the same ZDT were also employed to estimate the uncertainty of strains derived from measured in-plane deformations. Fig. B1c shows the strains of Specimen ED1V100 for a subset, step and filter size of 21 px, 6 px and 15 data points, respectively, averaged for 6x18 quadratic cells. The filter size describes the number of deformation data points (steps) used to derive the strain of a point of concern [48]. Fig. B1d supplies an overview of the 6x18 cells concerning the uncertainty related to the choice of the filter size: the standard deviation is rather high (average of all cells > 100 microstrains) when relying on a filter size of 5 data points, which corresponds to a virtual gauge length of 1.8 mm. However, it distinctly decreases when increasing the filter size to 15 data points. The standard deviation for both principal strains ε_1 and ε_2 is identical (coinciding curves in Fig. B.1d). Note that the ZDT cannot capture the bias related to deformations during the test [48]. However, the relevant deformations in the presented push-off tests are below 1 mm. Therefore, they presumably generate only a minor bias, making the ZDT roughly representative for evaluating the uncertainty of provided strains.
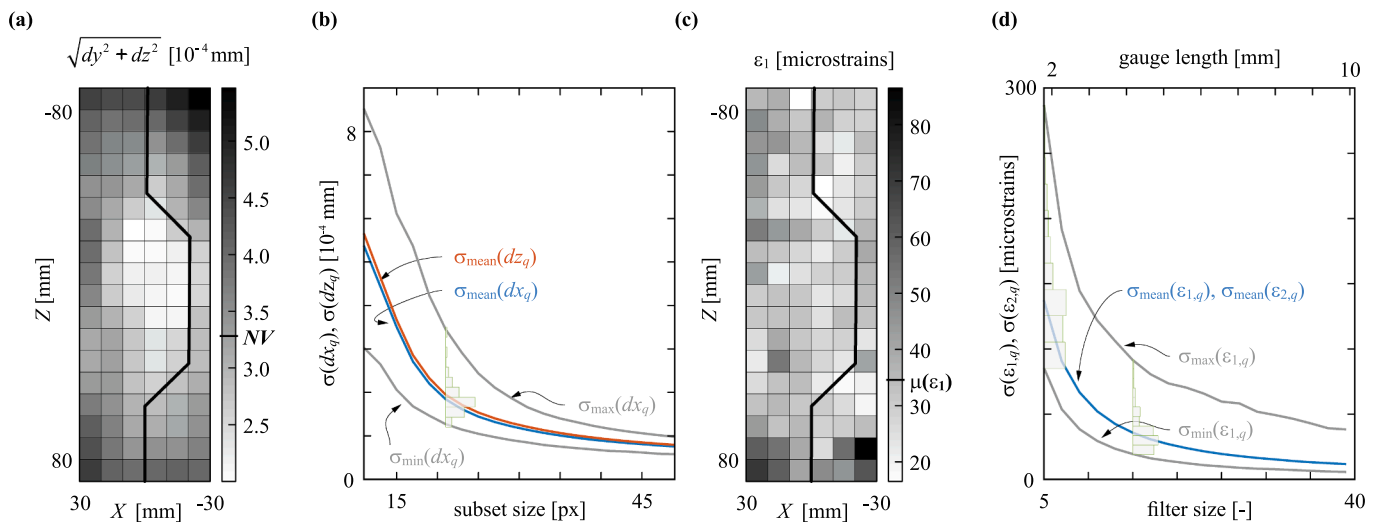

Fig. B1. Results of the DIC uncertainty quantification with a zero displacement test for specimen ED1V100: (a) measured in-plane deformation averaged per cell for subset size = 21 px and step size = 6 px with NV = 0.33 μm (6x18 cells according to VDI 2626 [48,63]); (b) standard deviation for in-plane displacements of all cells in function of subset size; (c) measured in-plane strains averaged per cell for subset size = 21 px, step size = 6 px and filter size = 15 with mean value $\mu(\varepsilon_1) = 35$ microstrains; (d) standard deviation for principal strains of all cells in function of filter size.
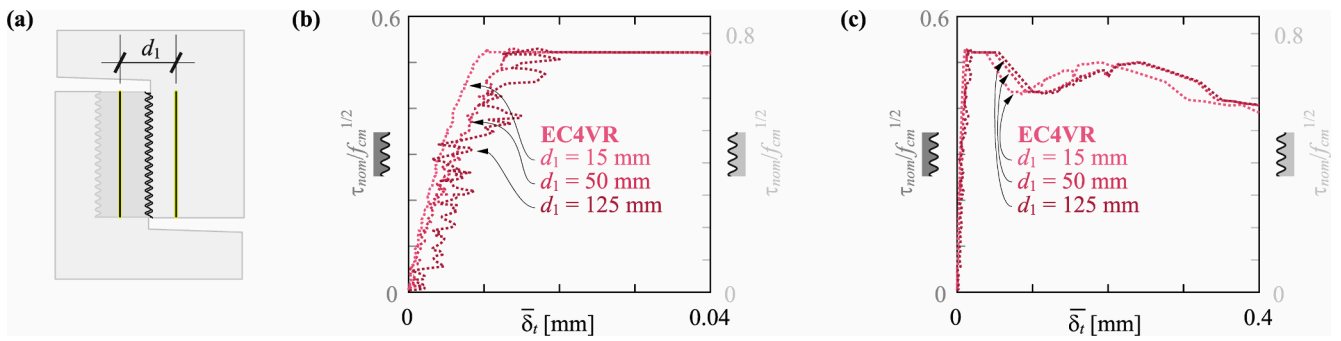
Fig. B2. Evaluation of push-off tests on DFC construction joints with varying measurement reference distance d_1: (a) reference distance d_1 used to measure the joint deformation δ_t and δ_n; (b) and (c) nominal shear stress τ_{nom} normalised with square root of concrete compressive strength $f_{cm}^{1/2}$ (left: f_{cm} of Eggshell insert, right: f_{cm} of contact piece) against average joint slip $\bar{\delta}_t$ for three different reference distances.

B.2. Joint kinematics

The reference length, perpendicular and parallel to the point of interest, used to determine the joint kinematics is highly relevant since, for the small relative displacements occurring up to the peak shear force, the deformations of the concrete next to the joint cannot be neglected. Fig. B2 illustrates the influence of varying the distance d_1 perpendicular to the joint for the average joint slip of Specimen EC4VR. Hence, the relative displacements measured by LVDTs, as often used in push-off tests, would have to be corrected to obtain the proper joint kinematics.

For deformations below 0.1 mm, the measured deformation can easily be 50% higher than if measured directly at the joint. Furthermore, Fig. C6b, Fig. C7b and Fig. C8 show that the joint slip may be almost constant along the tested length; however, Fig. C6c, Fig. C7c and Fig. C8 indicate that the joint opening varies over the joint height, with negative values at the edges and the maximum opening at the centre.

B.3. Principal strains and directions

To evaluate the principal strains and their directions, a median time filter including 15 data points (hence, ±3.5 s for each measurement point) was applied to reduce noise. Furthermore, after calculating the strains with a small spatial filter size of 5 data points (corresponding virtual gauge length = 1.8 mm, see Appendix B.1), all measurement points whose calculated principal tensile strain at the peak load exceeded 1500 microstrains were excluded from the evaluation as soon as their calculated strain exceeded 400 microstrains; the excessively high tensile strains of these points may have been caused by (i) crack and joint displacements, (ii) insufficient speckle quality, or both. The remaining data points were consolidated by averaging the spatial data with a window size of 15 data points for the evaluations presented in Section 4 and Appendix C and either 15 or 45 data points for the evaluation presented in Appendix A. This process resulted from optimising (i) the virtual gauge length to retain a high resolution and (ii) the measurement uncertainty to approximately an order of magnitude smaller than expected deformations in the actual test to minimise noise.

The principal strains and directions shown in Fig. 11, Fig. C6 and Fig. C7 resulted from post-processing high-resolution DIC measurements at 2 mm below the loaded end of the key (Fig. 11, dry keyed joints) and directly at the joint (Fig. C6 and Fig. C7, construction joints). The measurement positions are indicated in the corresponding figures. Note that the evaluated results represent highly concentrated but still averaged information. Fig. B3 illustrates that both the magnitude and direction of the principal strains vary slightly within the considered area (e.g. consider Fig. B3c).
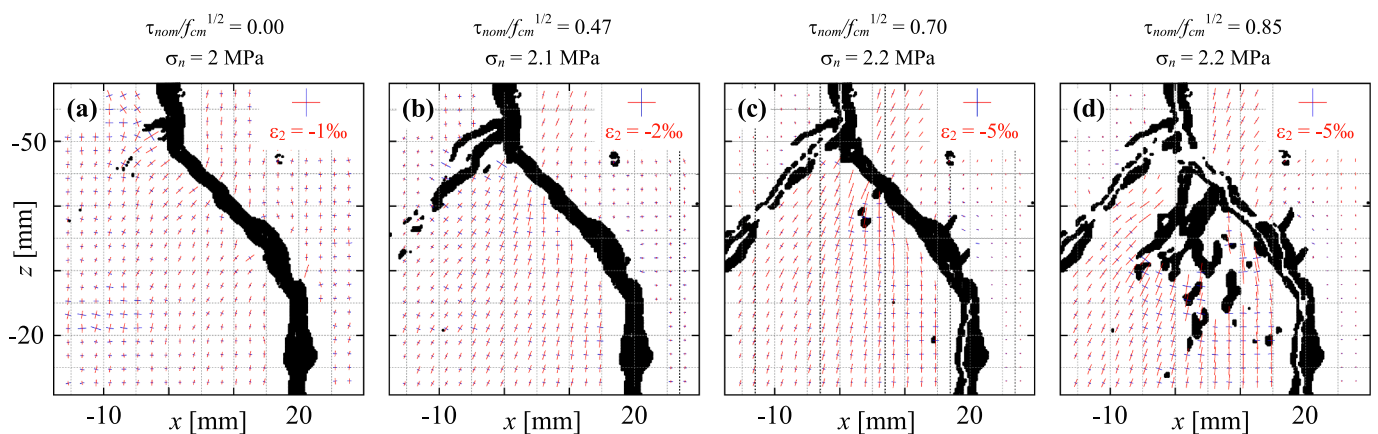
Fig. B3. Orientation and magnitude of principal strains ε_1 and ε_2 at the loaded end of the key determined from high-resolution full-field displacements from DIC measurements for Specimen ED1V100 (the black hatch indicates the locations with unrealistically high tensile strains.

Appendix C. Additional experimental results

C.1. Description of construction joint surface

This section provides detailed information on the surface scans for Specimens EC4H (Fig. C1), EC4V (Fig. C2), EC2H (Fig. C3) and EC2HR (Fig. C4). The statistical summary of this information is provided in Table 1.

The evaluation of the construction joint surface indicates that the overall depth of the formwork corrugation was smaller than planned: the "valleys" and "mountains" of the corrugation deviate from the model geometry. Furthermore, Fig. C1 and Fig. C3 evidence that the formwork bulged slightly at the top of horizontally printed formworks due to the hydrostatic pressure during casting (bulging of approximately 0.5 mm). Finally, the surface scans identified air included in the formwork (e.g. see Fig. C1a at $y = 3$ mm and $z = -83$ mm) and some pieces broken off while removing the formwork (e.g. see Fig. C2a at $y = -45...-20$ mm and $z = -77$ mm).

C.2. High-resolution measurements in construction joints

Fig. C6 and Fig. C7 provide detailed information for Specimens EC4H and EC2H on (i) the slip and opening over the height of the joint for three different load steps marked in Fig. C5 (load steps A, B and C) and (ii) the magnitude and direction of the principal compressive strains at three locations (area 1, 2 and 3) of the corrugation.

The joint slip δ_t, shown in Fig. C6b and Fig. C7b, was approximately constant over the height. Even though the measured slip was close to the measurement uncertainty, it can be seen that the corrugation affected the value of the local slip since the slip tended to be smaller in the inclined sections of the corrugation and larger slip in the valleys and mountains of the corrugation. On the other hand, the joint opening δ_n is larger at the centre and negative (i.e. denoting compressive strains between the reference points) at the edges.

The orientation and magnitude of principal compressive strains (hence the transferred compressive stresses) at the corrugated joint interface confirm that the shear transfer is more pronounced where the joint opening is smaller (see Fig. C6d and Fig. C7d). Note that the overall transferred force was not higher for EC4H than EC2H despite the higher compressive strains at higher joint slip δ_t (the strains at equal joint slip δ_t were almost identical). The strain state in the zone with "negative joint opening" could not be evaluated because the corrugation could not be identified in this compressed area with the DIC measurement.

For the reinforced construction joints, the joints of Specimens EC2HR and EC4HR slightly tilted beyond the shear transfer capacity mobilised by adhesion and mechanical interlock, as identified in Fig. C8b-c and Fig. C8f-g. This tilting could not be correlated to the slight force differences measured in the four restraining rods. The joint of Specimen EC4VR remained well oriented (see Fig. C.8d and Fig. C.8h), also at higher joint displacements exceeding the range shown in Fig. C.8.
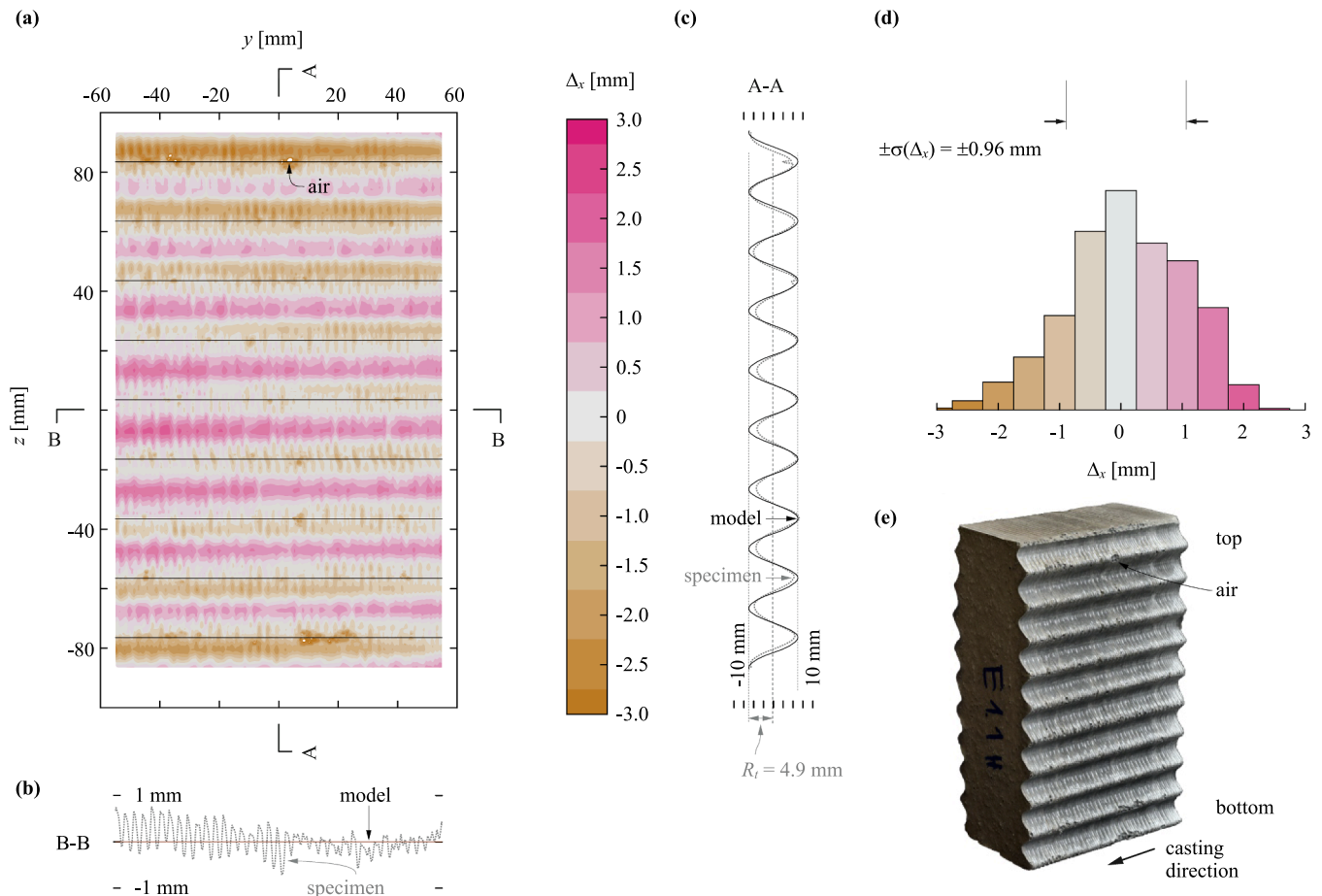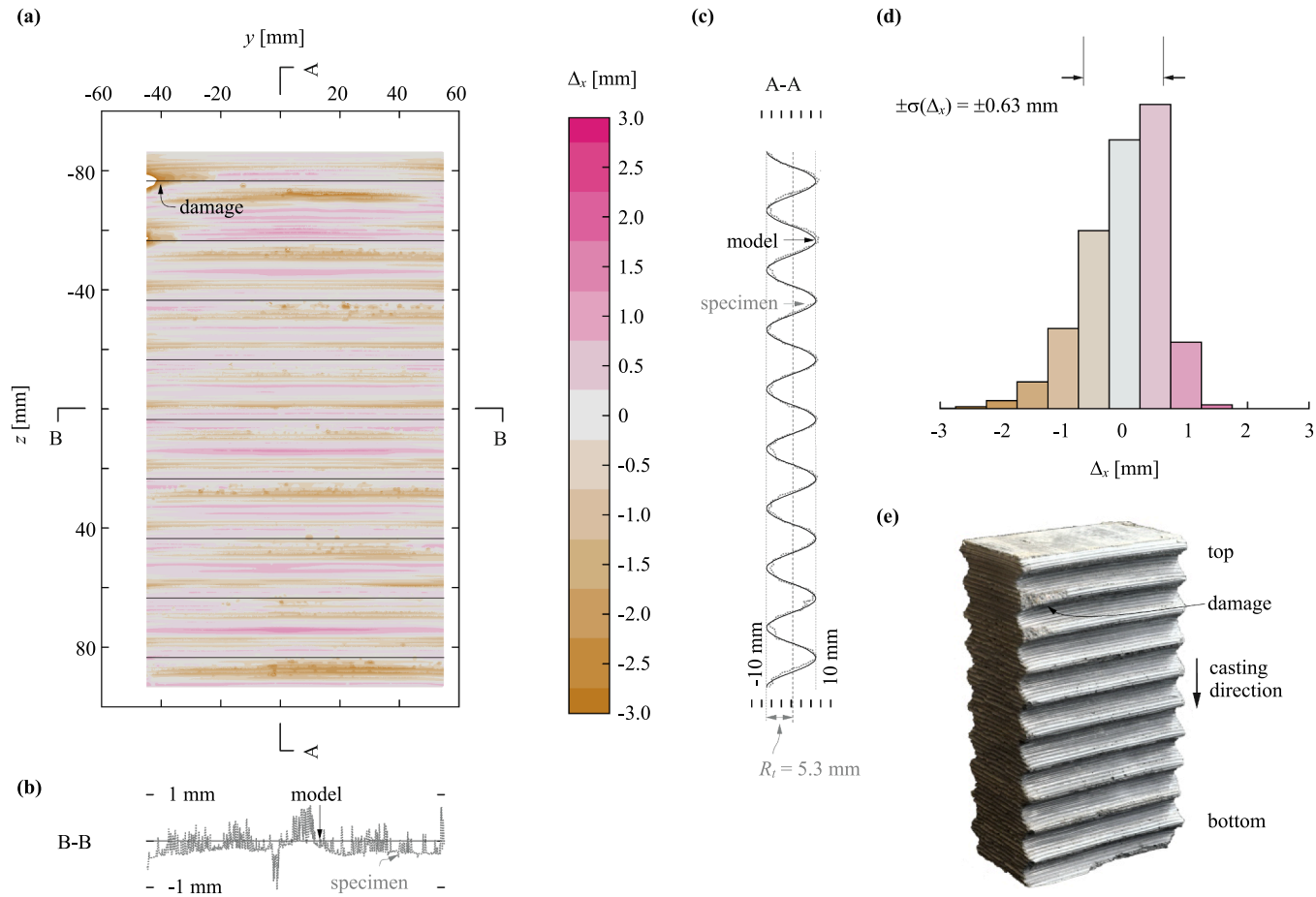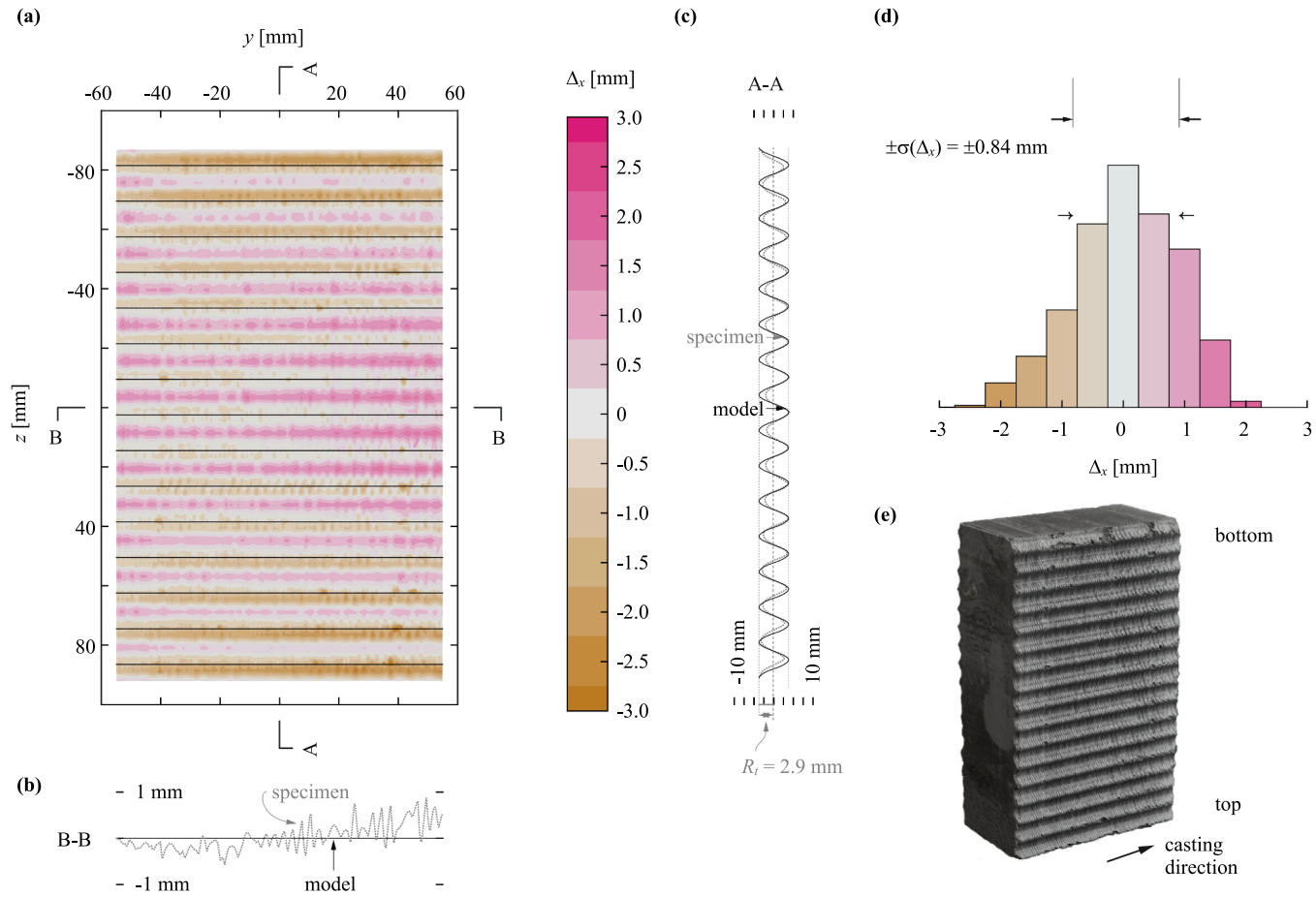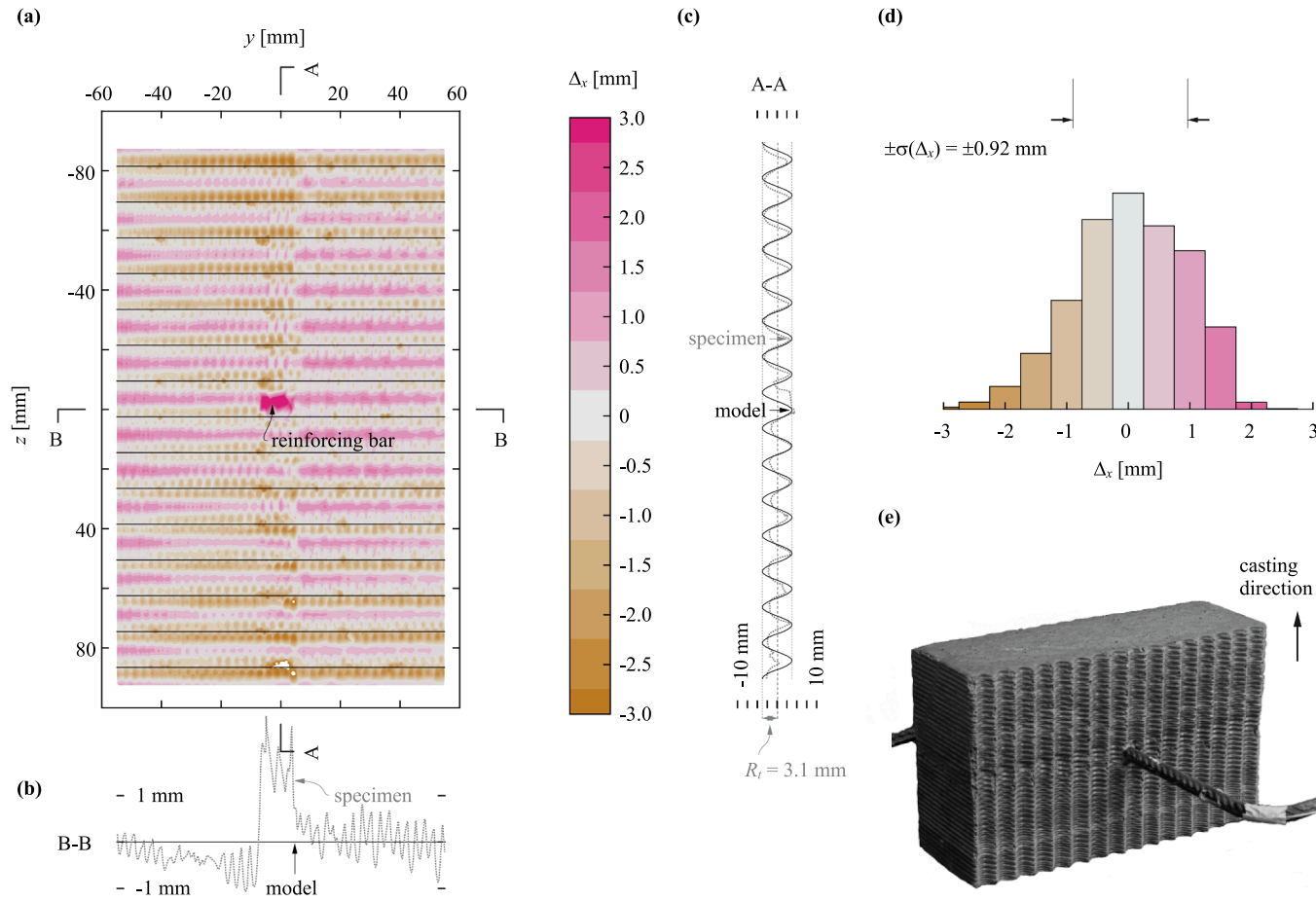

Fig. C1. Comparison of the model geometry and the scanned surface for Specimen EC4H: (a) overall geometrical deviations Δ_x; (b) horizontal section (y-direction); (c) vertical section (z-direction); (d) histogram of deviations; (e) photo of the insert after formwork removal.

Fig. C2. Comparison of the model geometry and the scanned surface for Specimen EC4V: (a) overall geometrical deviations Δ_x; (b) horizontal section (y-direction); (c) vertical section (z-direction); (d) histogram of deviations; (e) photo of the insert after formwork removal.

Fig. C3. Comparison of the model geometry and the scanned surface for Specimen EC2H: (a) overall geometrical deviations Δ_x; (b) horizontal section (y-direction); (c) vertical section (z-direction); (d) histogram of deviations; (e) photo of the insert after formwork removal.

Fig. C4. Comparison of the model geometry and the scanned surface for Specimen EC2HR: (a) overall geometrical deviations Δ_x; (b) horizontal section (*y*-direction); (c) vertical section (*z*-direction); (d) histogram of deviations; (e) photo of the insert after formwork removal.
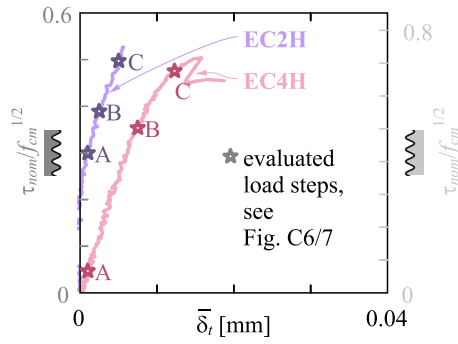
Fig. C5. Definition of evaluated load steps A, B and C for Specimens EC4H and EC2H in Fig. C.6 and Fig. C.7, respectively.
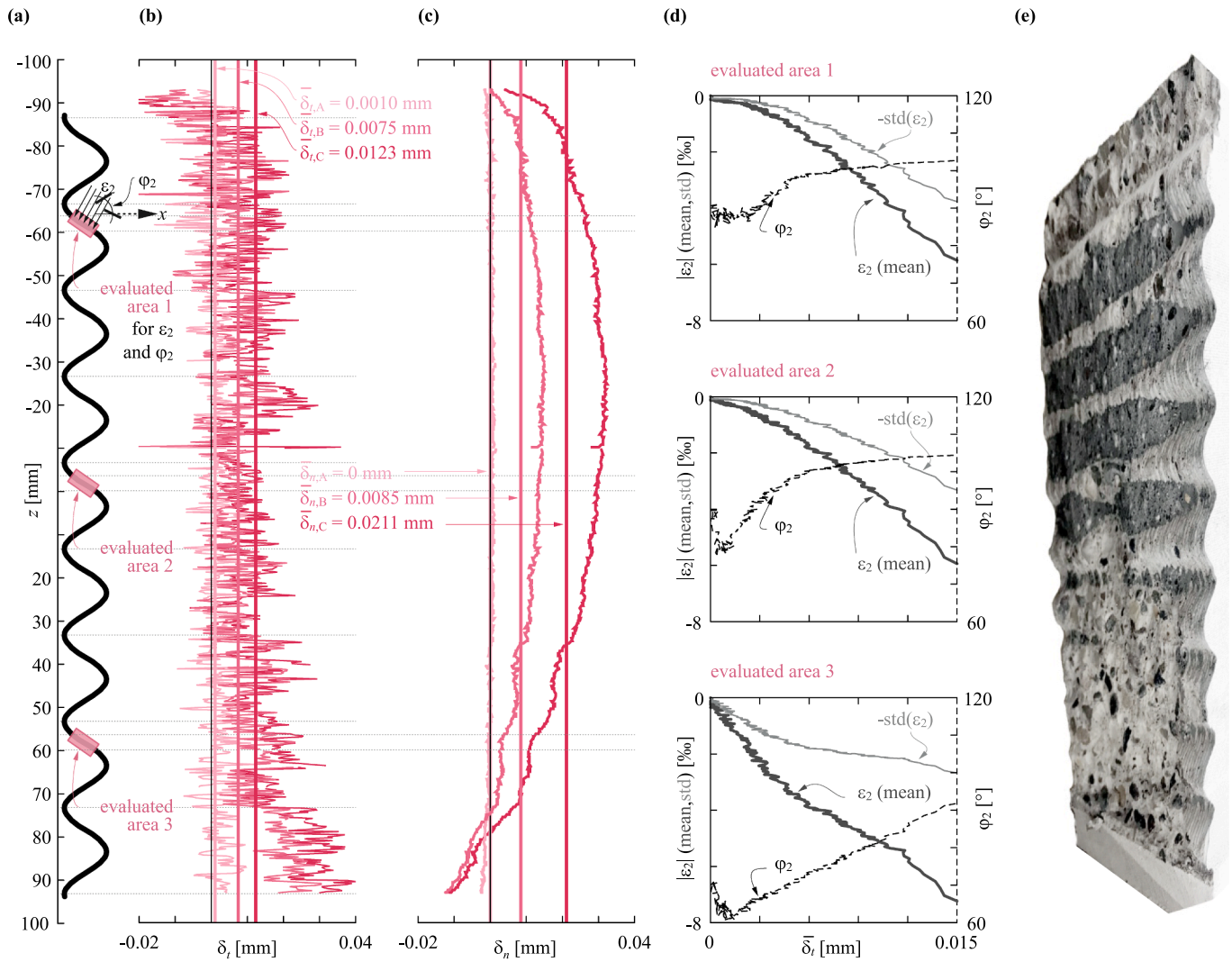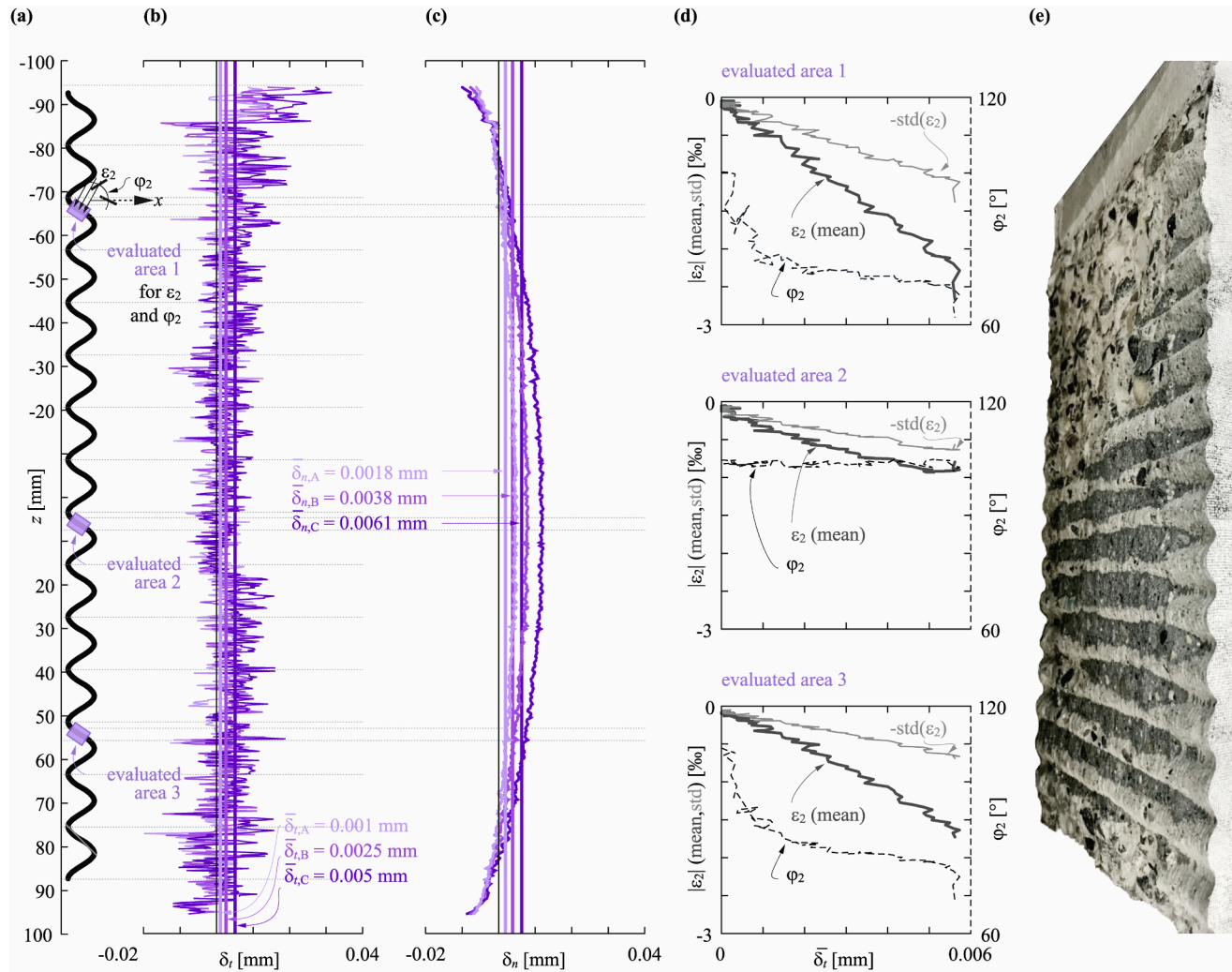

Fig. C6. High-resolution DIC measurements at joint of Specimen EC4H: (a) joint surface with indication of areas for local analysis of ε_2 and φ_2 (measured from x-direction); (b) joint slip δ_t over height z at average slips $\bar{\delta}_{t,A} = 0.001$ mm, $\bar{\delta}_{t,B} = 0.0075$ mm and $\bar{\delta}_{t,C} = 0.0123$ mm; (c) joint opening δ_n over height z at $\bar{\delta}_{t,A}$, $\bar{\delta}_{t,B}$ and $\bar{\delta}_{t,C}$; (d) principal compressive strain ε_2 as well as corresponding direction φ_2, against the average joint slip $\bar{\delta}_t$ on the evaluated areas 1...3 indicated in (a); (e) photo of failed joint.

Fig. C7. High-resolution DIC measurements at joint of Specimen EC2H: (a) joint surface with indication of areas for local analysis of ε_2 and φ_2 (measured from x-direction); (b) joint slip δ_t over height z at average slips $\bar{\delta}_{t,A} = 0.001$ mm, $\bar{\delta}_{t,B} = 0.0025$ mm and $\bar{\delta}_{t,C} = 0.005$ mm; (c) joint opening δ_n over height z at $\bar{\delta}_{t,A}, \bar{\delta}_{t,B}$ and $\bar{\delta}_{t,C}$; (d) principal compressive strain ε_2 as well as corresponding direction φ_2, against the average joint slip $\bar{\delta}_t$ In the evaluated areas 1...3 indicated in (a); (e) photo of failed joint.
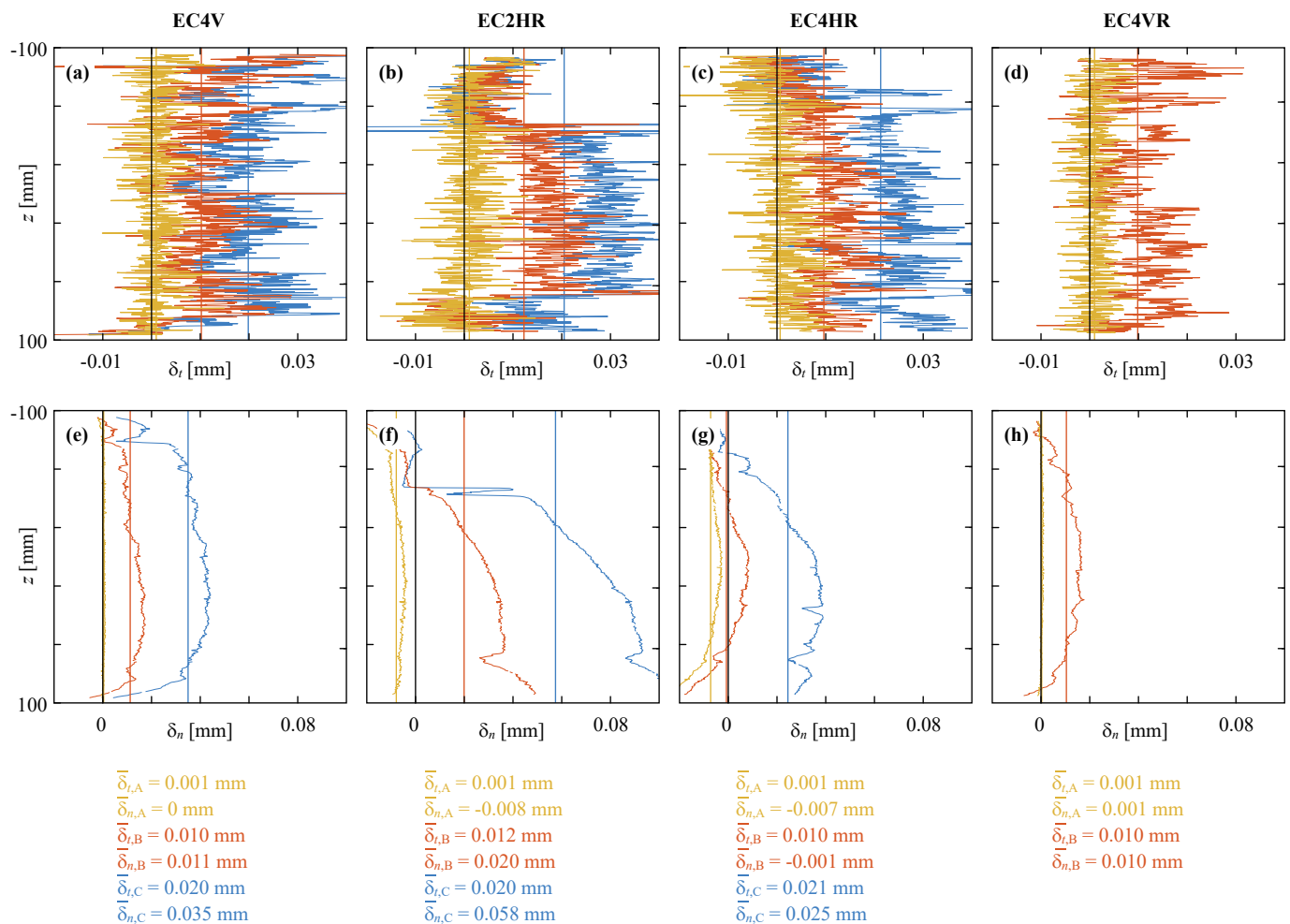
Fig. C8. Joint slip δ_t and joint opening δ_n over height z at average slips of approximately $\bar{\delta}_{t,A} = 0.001$ mm, $\bar{\delta}_{t,B} = 0.010$ mm and $\bar{\delta}_{t,C} = 0.020$ mm: (a) Specimen EC4V; (b) EC2HR; (c) EC4HR; (d) EC4VR.

References

[1] Engström B, et al. fib Bulletin 43. Structural connections for precast concrete buildings. fib. The International Federation for Structural Concrete, 2008. 10.35789/fib.BULL.0043.

[2] Gibson I, Rosen D, Stucker B. Introduction and Basic Principles. In: Gibson I, Rosen D, Stucker B, editors. Additive Manufacturing Technologies: 3D Printing, Rapid Prototyping, and Direct Digital Manufacturing. New York, NY: Springer; 2015. p. 1–18. https://doi.org/10.1007/978-1-4939-2113-3_1.

[3] Wangler T, Roussel N, Bos FP, Salet TAM, Flatt RJ. Digital Concrete: A Review. Cem Concr Res Sep. 2019;123:105780. https://doi.org/10.1016/j.cemconres.2019.105780.

[4] Mata-Falcón J, Bischof P, et al. Digitally fabricated ribbed concrete floor slabs: a sustainable solution for construction. RILEM Technical Letters Sep 2022;7:68–78. https://doi.org/10.21809/rilemtechlett.2022.161.

[5] Anton A, Skevaki E, Bischof P, Reiter L, Dillenburger B. Design, Fabrication and Assembly Strategies for 3D Concrete Printed Column - Slab Interfaces. presented at the 42nd Annual Conference of the Association for Computer Aided Design in Architecture (ACADIA 2022), Philadelphia, 2022.

[6] Nuh M, Oval R, Orr J, Shepherd P. Digital fabrication of ribbed concrete shells using automated robotic concrete spraying. Addit Manuf Nov. 2022;59. https://doi.org/10.1016/j.addma.2022.103159. p. 103159.

[7] Burger J, Huber T, Lloret-Fritschi E, Mata-Falcón J, Gramazio F, Kohler M. Design and fabrication of optimised ribbed concrete floor slabs using large scale 3D printed formwork. Autom Constr Dec. 2022;144:104599. https://doi.org/10.1016/j.autcon.2022.104599.

[8] Huber T, Burger J, Mata-Falcón J, Kaufmann W. Structural design and testing of material optimised ribbed RC slabs with 3D printed formwork. fib Structural Concrete 2023. https://doi.org/10.1002/suco.202200633.

[9] C. Chastre Rodrigez et al., fib Bulletin 74. Planning and design handbook on precast building structures. fib. The International Federation for Structural Concrete, 2014. 10.35789/fib.BULL.0074.

[10] International Federation for Structural Concrete, 'Interface Characteristics. In: fib Model Code for Concrete Structures 2010, Berlin: Ernst & Sohn, 2013, p. 152–89. 10.1002/9783433604090.ch6.

[11] R. Reinecke, 'Haftverbund und Rissverzahnung in unbewehrten Betonschubfugen', Dissertation, Technische Universität München, München, 2004.

[12] Baghdadi A, Meshkini A, Kloft H. Inspiration of Interlocking Wooden Puzzles for Precast Concrete Construction. In: Proceedings of the International fib Symposium on the Conceptual Design of Structures , Switzerland, Attisholz Areal, Switzerland, 2021, p. 531–8.

[13] Bischof P, Mata-Falcón J, Kaufmann W. Fostering innovative and sustainable mass-market construction using digital fabrication with concrete. Cem Concr Res Nov. 2022;161:106948. https://doi.org/10.1016/j.cemconres.2022.106948.

[14] Hack N, Kloft H. Shotcrete 3D Printing Technology for the Fabrication of Slender Fully Reinforced Freeform Concrete Elements with High Surface Quality: A Real-Scale Demonstrator. Ini Second RILEM International Conference on Concrete and Digital Fabrication, Cham, 2020, pp. 1128–1137. 10.1007/978-3-030-49916-7_107.

[15] Muñiz MM, et al. Concrete hybrid manufacturing: A machine architecture. Procedia CIRP Jan. 2021;97:51–8. https://doi.org/10.1016/j.procir.2020.07.003.

[16] Nielsen CV. Triaxial Behavior of High-Strength Concrete and Mortar. MJ, vol. 95, no. 2, pp. 144–151, Mar. 1998, 10.14359/359.

[17] Sørensen JH. Design and Modeling of Structural Joints in Precast Concrete Structures. Copenhagen: Technical University of Denmark, Department of Civil Engineering; 2018. Doctoral Thesis. Accessed: Mar. 22, 2023 [Online]. Available: https://orbit.dtu.dk/en/publications/design-and-modeling-of-structural-joints-in-precast-concrete-stru.

[18] Bischof P, Mata-Falcón J, Ammann R, Näsbom A, Kaufmann W. Digitally fabricated weak interfaces to reduce minimum reinforcement in concrete structures, fib Struct. Concr., Dec 2022. https://doi.org/10.1002/suco.202200732.

[19] Gebhard L, Mata-Falcón J, Anton A, Dillenburger B, Kaufmann W. Structural behaviour of 3D printed concrete beams with various reinforcement strategies. Eng Struct Aug. 2021;240:112380. https://doi.org/10.1016/j.engstruct.2021.112380.

[20] Gebhard L, et al. Towards efficient concrete structures with ultra-thin 3D printed formwork: exploring reinforcement strategies and optimisation. Virtual Phys

Prototyping Jul. 2022;17(3):599–616. https://doi.org/10.1080/17452759.2022.2041873.

[21] Burger J, Lloret-Fritschi E, et al. Eggshell: Ultra-Thin Three-Dimensional Printed Formwork for Concrete Structures. 3D Printing Addit Manuf Apr. 2020;7(2):48–59. https://doi.org/10.1089/3dp.2019.0197.

[22] Lloret E, et al. Complex concrete structures: Merging existing casting techniques with digital fabrication. Comput Aided Des Mar. 2015;60:40–9. https://doi.org/10.1016/j.cad.2014.02.011.

[23] Birkeland PW, Birkeland HW. Connections in Precast Concrete Construction. ACI J Proc 1966;63(3). Art. no. 42.

[24] Mattock AH, Hawkins NM. Shear Transfer In Reinforced Concrete - Recent Research. PCI J. 1972;17(2):55–75. 10.15554/pcij.03011972.55.75.

[25] Mattock AH. 'Shear Transfer Under Monotonic Loading, Across an Interface Between Concretes Cast at Different Times'., Washington Univ., Seattle. Washington, D.C.: Dept. of Civil Engineering.; National Science Foundation; 1976. PB275257.

[26] Randl N. Design recommendations for interface shear transfer in fib Model Code 2010. Struct Concr 2013;14(3):230–41. https://doi.org/10.1002/suco.201300003.

[27] Lange DA, Jennings HM, Shah SP. Relationship between Fracture Surface Roughness and Fracture Behavior of Cement Paste and Mortar. J Am Ceram Soc 1993;76(3):589–97. https://doi.org/10.1111/j.1151-2916.1993.tb03646.x.

[28] Kaufmann N. Das Sandflächenverfahren. Straßenbautechnik 1971;24(3).

[29] Brenni P. 'Il comportamento al taglio di una struttura a sezione mista in calcestruzzo e getti successivi', Doctoral Thesis. ETH Zurich 1995. https://doi.org/10.3929/ethz-a-001460035.

[30] Tirassa M, Fernández Ruiz M, Muttoni A. Influence of cracking and rough surface properties on the transfer of forces in cracked concrete. Eng Struct Dec. 2020;225:111138. https://doi.org/10.1016/j.engstruct.2020.111138.

[31] Lenz P. Beton-Beton-Verbund. Technische Universität München; 2012. Doctoral Thesis, Apr. 21, 2022. Accessed: Mar. 22, 2023 [Online]. Available: http://mediatum.ub.tum.de/node?id=1106588.

[32] Etter S. 'Zum Tragverhalten von Verbundbauteilen aus altem und neuem Stahlbeton', Doctoral Thesis. ETH Zurich 2012. https://doi.org/10.3929/ethz-a-007608487.

[33] Martens R. 'Zum Tragverhalten von Betonplatten mit integrierten Schalungselementen', Doctoral Thesis. ETH Zurich 1997. https://doi.org/10.3929/ethz-a-001853800.

[34] EN 1992-1-1, 'Eurocode 2: Design of concrete structures - Part 1-1: General rules and rules for buildings', Brussels, 2004.

[35] Koseki K, Breen JE. Exploratory Study of Shear Strength of Joints for Precast Segmental Bridges. University of Texas, Austin, Texas State Department of Highways & Public Transportation and Federal Highway Administration, Austin, Intrm Rpt. FHWA-TX-84-32+248-1, 1983. Accessed: Mar. 22, 2023 [Online]. Available: https://trid.trb.org/view/200691.

[36] Buyukozturk O, Bakhoum MM, Michael Beattie S. Shear Behavior of Joints in Precast Concrete Segmental Bridges. J Struct Eng. Dec. 1990;116(12);Art. no. 12. 10.1061/(ASCE)0733-9445(1990)116:12(3380).

[37] Kaneko Y, Connor JJ, Triantafillou TC, Leung CK. Fracture Mechanics Approach for Failure of Concrete Shear Key. I: Theory. J Eng Mech Apr. 1993;119(4):681–700. https://doi.org/10.1061/(ASCE)0733-9399(1993)119:4(681).

[38] Figueira D, Sousa C, Calçada R, Serra Neves A. Design recommendations for reinforced concrete interfaces based on statistical and probabilistic methods. Struct Concr 2016;17(5):811–23. https://doi.org/10.1002/suco.201500083.

[39] AASHTO, 'Guide specification for design and construction of segmental concrete bridges, 2nd Ed.', Washington, DC., 1999.

[40] M. M. Bakhoum, 'Shear behavior and design of joints in precast concrete segmental bridges', Thesis, Massachusetts Institute of Technology, 1990. Accessed: Mar. 22, 2023 [Online]. Available: https://dspace.mit.edu/handle/1721.1/13685.

[41] Specker A. Der Einfluss der Fugen auf die Querkraft- und Torsionstragfähigkeit extern vorgespannter Segmentbrücken, Doctoral thesis, Technische Universität

Hamburg-Harburg, 2001. Accessed: Mar. 22, 2023 [Online]. Available: https://doi.org/10.15480/882.1060.

[42] Kupfer H, Guckenberger K, Daschner F. Versuche zum Tragverhalten von segmentären Spannbetonträgern. DAfStb 1982;no. 335.

[43] Zhou X, Mickleborough N, Li Z. Shear Strength of Joints in Precast Concrete Segmental Bridges. ACI Struct J 2005;102(1). 3-11. doi:10.14359/13525.

[44] Mitropoulou I, Burger J, Casas G, Jipa A, Bernhard M, Mele TV. compas-dev/compas_slicer: 0.5.0. Zenodo Jan. 27, 2022. https://doi.org/10.5281/zenodo.5910846.

[45] Jipa A, Dillenburger B. 3D Printed Formwork for Concrete: State-of-the-Art, Opportunities, Challenges, and Applications. 3D Printing Addit Manuf Apr. 2022;9 (2):84–107. https://doi.org/10.1089/3dp.2021.0024.

[46] Marti P. Size Effect in Double-Punch Tests on Concrete Cylinders. MJ Nov. 1989;86 (6):597–601. https://doi.org/10.14359/2261.

[47] Li B, Maekawa K, Okamura H. Contact density model for stress transfer across cracks in concrete. J Faculty Eng, Univ Tokyo 1989;40:9–52.

[48] Mata-Falcón J, Haefliger S, Lee M, Galkovski T, Gehri N. Combined application of distributed fibre optical and digital image correlation measurements to structural concrete experiments. Eng Struct Dec. 2020;225:111309. https://doi.org/10.1016/j.engstruct.2020.111309.

[49] Gehri N, Mata-Falcón J, Kaufmann W. Automated crack detection and measurement based on digital image correlation. Constr Build Mater Sep. 2020; 256:119383. https://doi.org/10.1016/j.conbuildmat.2020.119383.

[50] Gehri N, Mata-Falcón J, Kaufmann W. Refined extraction of crack characteristics in large-scale concrete experiments based on digital image correlation. Eng Struct Jan. 2022;251:113486. https://doi.org/10.1016/j.engstruct.2021.113486.

[51] Luna Inc., 'Fiber Optic Sensing and Measurement Systems', Luna Innovations, 2022. https://www.lunainc.com (accessed Jun. 12, 2022).

[52] Galkovski T, Lemcherreq Y, Mata-Falcón J, Kaufmann W. Fundamental Studies on the Use of Distributed Fibre Optical Sensing on Concrete and Reinforcing Bars. Sensors 2021;21(22). https://doi.org/10.3390/s21227643.

[53] Lemcherreq Y, Galkovski T, Mata-Falcón J, Kaufmann W. Application of Distributed Fibre Optical Sensing in Reinforced Concrete Elements Subjected to Monotonic and Cyclic Loading. Sensors 2022;22(5). https://doi.org/10.3390/s22052023.

[54] Rombach GA, Abendeh R. Bow-shaped segments in precast segmental bridges. Eng Struct Jun. 2008;30(6):1711–9. https://doi.org/10.1016/j.engstruct.2007.11.012.

[55] Kaneko Y, Connor JJ, Triantafillou TC, Leung CK. Fracture Mechanics Approach for Failure of Concrete Shear Key. II: Verification. J Eng Mech Apr. 1993;119(4): 701–19. https://doi.org/10.1061/(ASCE)0733-9399(1993)119:4(701).

[56] Wang L, Yang Y, Yao L, Ma G. Interfacial bonding properties of 3D printed permanent formwork with the post-casted concrete. Cem Concr Compos Apr. 2022; 128:104457. https://doi.org/10.1016/j.cemconcomp.2022.104457.

[57] prEN 1992-1-1:2022, 'Eurocode 2: Design of concrete structures - Part 1-1: General rules and rules for buildings', Brussels, 2022.

[58] Zanotti C, Randl N. Are concrete-concrete bond tests comparable? Cem Concr Compos May 2019;99:80–8. https://doi.org/10.1016/j.cemconcomp.2019.02.012.

[59] Giraldo Soto A, Kaufmann W. Effect of Test Setups on the Shear Transfer Capacity Across Cracks in FRC. In: Fibre Reinforced Concrete: Improvements and Innovations, Cham, 2021, p. 163–175. 10.1007/978-3-030-58482-5_15.

[60] Sørensen JH, Hoang LC, Poulsen PN. Keyed shear connections with looped U-bars subjected to normal and shear forces Part I: Experimental investigation. Struct Concr 2021;22(4). https://doi.org/10.1002/suco.202000727.

[61] Echegaray-Oviedo J, Navarro-Gregori J, Cuenca E, Serna P. Modified push-off test for analysing the shear behaviour of concrete cracks. Strain 2017;53(6). https://doi.org/10.1111/str.12239. Art. no. 6.

[62] Correlated Solutions, 'VIC-3D'. https://www.correlatedsolutions.com/vic-3d/ (accessed Jun. 12, 2022).

[63] Fachbereich Prozessmesstechnik und Strukturanalyse. 'VDI/VDE 2626 Blatt 1 - Optische Messverfahren - Bildkorrelationsverfahren - Grundlagen und Begriffe'. VDI/VDE-Gesellschaft Mess- und. Automatisierungstechnik 2018.